JACS
JOURNAL OF THE AMERICAN CHEMICAL SOCIETY

Article

Functional Models for the Mono- and Di-nitrosyl Intermediates of FNORs: Semireduction versus Superreduction of NO

Manish Jana, Corey J. White, Nabhendu Pal, Serhiy Demeshko, Claudia Kupper, Franc Meyer, Nicolai Lehnert, and Amit Majumdar

J. Am. Chem. Soc., **Just Accepted Manuscript** • DOI: 10.1021/jacs.9b13795 • Publication Date (Web): 13 Mar 2020

Just Accepted

is published by the American Chemical Society. 1155 Sixteenth Street N.W., Washington, DC 20036

Functional Models for the Mono- and Di-nitrosyl Intermediates of FNORs: Semireduction versus Superreduction of NO

Manish Jana,[†] *Corey J. White,*[‡ǂ] *Nabhendu Pal,*[†ǂ] *Serhiy Demeshko,*[§] *Claudia Cordes (née Kupper),*[§] *Franc Meyer,*[§] *Nicolai Lehnert,**[‡] *and Amit Majumdar**[†]

[†]School of Chemical Sciences, Indian Association for the Cultivation of Science, 2A & 2B Raja S. C. Mullick Road, Jadavpur, Kolkata 700032, West Bengal, India

[‡]Department of Chemistry, The University of Michigan, 930 N. University Ave., Ann Arbor, Michigan 48109, United States

[§] Institut für Anorganische Chemie, Georg-August-Universität, Tammannstraße 4, 37077 Göttingen, Germany

[ǂ]These authors contributed equally

*E-mail: [‡]lehnertn@umich.edu, [†]icam@iacs.res.in

ABSTRACT: The reduction of NO to N_2O by flavodiiron nitric oxide reductases (FNORs) is related to the disruption of the defense mechanism in mammals against invading pathogens. The proposed mechanism for this catalytic reaction involves both non-heme mono- and dinitrosyl diiron(II) species as the key intermediates. Recently, we have reported an initial account for NO reduction activity of an unprecedented mononitrosyl diiron(II) complex, $[Fe_2(N\text{-Et-HPTB})(NO)(DMF)_3](BF_4)_3$ (**1**) with $[Fe^{II}\{FeNO\}^7]$ formulation (Jana et al., *J. Am. Chem. Soc.* **2017**, *139*, 14380−14383). Here we report the full account for the selective synthesis, characterization and reactivity of FNOR model complexes, which include a dinitrosyl diiron(II) complex, $[Fe_2(N\text{-Et-HPTB})(NO)_2(DMF)_2](BF_4)_3$ (**2**) with $[\{FeNO\}^7]_2$ formulation and a related, mixed-valent diiron(II, III) complex, $[Fe_2(N\text{-Et-HPTB})(OH)(DMF)_3](BF_4)_3$ (**3**). Importantly, whereas complex **2** is able to produce 89% of N_2O via a semireduced mechanism (1 equiv. of $CoCp_2$ per dimer = 50% of NO reduced), complex **1**, under the same conditions (0.5 equiv. of $CoCp_2$ per dimer = 50% of NO reduced), generates only ~50% of N_2O. The mononitrosyl complex therefore requires superreduction for quantitative N_2O generation, which constitutes an interesting dichotomy between **1** and **2**. Reaction products obtained after N_2O generation by **2** using 1 and 2 eq. of reductant have been characterized by molecular structure determination and EPR spectroscopy. Despite several available literature reports on N_2O generation by diiron complexes, this is the first case where the end products from these reactions could be characterized unambiguously, which clarifies a number of tantalizing observations about the nature of these products in the literature.

INTRODUCTION

Nitric oxide (NO) is generated endogenously in mammals, and at nanomolar concentrations it plays a major role in nerve signal transduction and blood pressure control. In addition, NO also acts as an important component in the defense mechanism of mammals against various invading pathogens.[1-4] Although up to micromolar concentration of NO can be produced by iNOS in the activated macrophages as a response to bacterial infection,[5-6] few microbes such as *T. maritima,*[7] *M. thermoacetica*[8] and *D. gigas*,[9] are able to reduce NO to the much less toxic, neuropharmacological agent and greenhouse gas, nitrous oxide (N_2O), by expressing the enzymes flavodiiron nitric oxide reductases (FNORs).[10-13] This NO reduction process protects the microbes from "nitrosative stress" under anaerobic growth conditions. Consequently, the pathogens can proliferate[14] in the human body and may cause harmful infections. FNORs therefore gain significant importance in bacterial pathogenesis, and understanding the mechanism of these enzymes may immensely contribute in finding new ways to counter bacterial infection.

FNORs are a subclass of a broader family of enzymes which is known as flavodiiron proteins (FDPs).[11] FDPs have been comparatively recently recognized within the class of enzymes which contain carboxylate bridged nonheme diiron active sites[15] and are found in bacteria, archaea as well as in few protozoa.[11, 16-26] FDPs are primarily oxygen scavenging enzymes which reduce O_2 to water, thereby protecting the microbes under oxidative stress. In addition to such oxygen scavenging activity, some of the FDPs show preferential activity towards two electron reduction of NO to N_2O and are classified as FNORs. Evidence for an inducible NO-metabolizing and NO-detoxifying activity in anaerobic E. coli has been reported.[27] Here, it has been demonstrated that FNORs are expressed as a direct response to the exposure of *E. coli* cells to NO, which supports the role of these enzymes in the defense mechanism for the bacteria.[14] Other examples of such preferential NO reduction activity have been reported for *Desulfovibrio vulgaris*,[28] *Desulfovibrio gigas*[18] and *Morella thermoacetica*.[29] The corresponding enzyme from the latter anaerobic bacterium revealed a six-fold higher catalytic efficiency for NO vs. O_2 reduction.[30] X-ray structure

determination of the active site of *D. gigas* FNOR[9] revealed two non-heme iron centers separated by a distance of 3.2-3.6 Å. One iron center is coordinated by a glutamate and two histidines, while the second iron center is coordinated by an aspartate, a histidine and a water-based ligand. A water-based ligand and a bridging aspartate complete the coordination spheres. This unsymmetrical coordination environment around the two iron centers, however, has been found to be functionally irrelevant by mutagenesis studies.[31] The non-bridging water derived ligand in the active sites of *M. thermoacetica*[8] and *T. maritima*[7] (PDB: 1VME) is replaced by an additional histidine, and thus provides an identical, four His coordination environment around the two iron centers. Additionally, a flavin (FMN) cofactor is found within close range (4−6 Å) of the active site to facilitate rapid electron transfer.

FNORs are efficient catalysts and a fast reduction of NO was observed for FNORs from *M. thermoacetica* (k_{cat}= 48 s^{-1}, K_m= 4μM)[30] and *D. vulgaris* (k_{cat}= 12 s^{-1}, K_m= 19 μM)[28] while much less efficient NO reduction was observed for the FDP from *T. maritima* (k_{cat}= 0.05 s^{-1}, K_m= 70 μM),[7] which primarily functions as an O_2-reductase *in vivo*. The four electron reduced active site ($FMNH_2$-$Fe^{II}Fe^{II}$) of FNOR mediates the two electron reduction of NO to N_2O. The mechanism for the catalytic reduction of NO to N_2O by FNORs is much debated[10] and both mono- and dinitrosyl diiron intermediates have been invoked in two different proposed mechanisms.[10-12, 32-35] A detailed discussion on four of the proposed mechanisms, namely, the semireduced (mixed-valent), superreduced, direct coupling (diferrous dinitrosyl) and the hyponitrite mechanism is available elsewhere.[10] Some recent reports support the formation of a mononitrosyl species as an intermediate in the catalytic cycle.[7-8, 36] These reports include the formation of a stable mononitrosyl adduct, formed by the addition of 1 equiv of NO per diiron(II) site of both FMN-free[8] and FMN-containing[36] flavodiiron proteins. A more recent study on the mechanism of FNORs, however, has shown that the NO reductase reaction indeed proceeds through the successive formation of mononitrosyl species, [Fe^{II}{FeNO}^{7}], and dinitrosyl species, [{FeNO}^{7}]$_2$, of which the former is not the catalytically active species for N–N bond formation.[33] This report[33] shows that the

diferrous-dinitrosyl species is actually the catalytically active species and is converted to a diferric species and N_2O. Here the Enemark- Feltham notation, $\{MNO\}^x$, is used to classify metal-nitrosyl complexes,[37] where x denotes the sum of iron-d and NO(π*) electrons. Extensive characterization by experimental methods as well as support from theoretical calculations revealed that the high-spin non-heme $\{FeNO\}^7$ species with S = 3/2 ground state should be described as a high-spin Fe^{III} (S = 5/2) center antiferromagnetically coupled to NO^- (S = 1).[38-45] This description is also in good agreement with literature reports.[46-50] Additional investigations involved structural and vibrational spectroscopic characterization of non-heme iron(II) nitrosyls and has provided evidence in favor of strong π donation from NO^- to Fe(III), which leads to a very covalent Fe–NO unit in high spin $\{FeNO\}^7$ complexes.[51] It has also been shown by one of us (N. L.) that covalency in the Fe–NO unit decreases upon one-electron reduction, and thus leads to a comparatively weaker Fe–NO bond.[52] While the high degree of covalency of the Fe–NO bond in $\{FeNO\}^7$ units leads to their stability, reduction to $\{FeNO\}^8$ may therefore serve as the activation process of such stable non-heme $\{FeNO\}^7$ centers for further reactivity,[52] for example, N_2O production or disproportionation.

In the semireduced mechanism, the $[\{FeNO\}^7]_2$ species is reduced by $FMNH_2$ to generate FMNH(·) and $[\{FeNO\}^7\{FeNO\}^8]$, which in turn produces N_2O and a mixed-valent Fe(II)Fe(III) complex. The latter species is then reduced by FMNH(·) to regenerate the diferrous unit, which can then again undergo nitrosylation to regenerate $[\{FeNO\}^7]_2$. Such a mechanism has very recently been shown to be operative in a functional model complex of FNORs.[53] In the superreduced mechanism,[11] the $[\{FeNO\}^7]_2$ intermediate is first reduced by $FMNH_2$ to generate $[\{FeNO\}^8]_2$ and FMN. The former then produces N_2O and a diferrous complex. The diferrous unit may again undergo nitrosylation to regenerate $[\{FeNO\}^7]_2$. N_2O generation by a mononuclear $\{FeNO\}^7$ complex[54] and a dinuclear mononitrosyl $[Fe^{II}\{FeNO\}^7]$ complex[55] have been reported to proceed via the superreduced mechanism, but in an **inter**molecular N-N coupling reaction. The direct coupling mechanism considers N_2O production by direct N–N coupling in

the $[\{FeNO\}^7]_2$ complex to generate a Fe^{III}–O–Fe^{III} intermediate, which is then reduced by two electrons to a diferrous species by $FMNH_2$. Here, the reduction is not considered to be necessary for activation of the $[\{FeNO\}^7]_2$ intermediate. This pathway was supported by the capability of deflavinated *T. maritima* FDP[7, 33, 56] to carry out a turnover of 2 eq. NO to 0.7 eq. N_2O, which suggests that the FMN cofactor may not have any catalytic role and that it rather just re-reduces the active site. The feasibility of this mechanism is further supported by recent model complex studies.[57]

While *T. maritima* FDP primarily serves as an O_2 scavenging enzyme with low NO reductase activity *in vivo*, two $[\{FeNO\}^7]_2$ model complexes[58-59] and one $[Fe^{II}\{FeNO\}^7]$ model complex[55] are known to be stable in solution. These complexes do not produce N_2O in the absence of external reductants and hence, it seems quite unclear whether the direct coupling mechanism reflects the actual mechanism of NO reduction *in vivo*. A recent computational study has described a detailed reaction mechanism for the reductive coupling of NO at the diiron active site of FNORs and involves a series of intermediates featuring bound hyponitrites.[60] Metal complexes of first row transition metals containing bound *trans*- and *cis*-hyponitrite have been reported in the literature[61-67] and a recent report by one of us (F.M.) demonstrates the isolation of a *cis*-hyponitrite intermediate which could produce N_2O upon protonation.[68] Very recently, linkage isomers of reduced Ni-nitrosyl complexes have been shown to serve as key species in the reduction of NO at monometallic sites to produce N_2O upon protonation of a cis-hyponitrite intermediate.[69]

Reactivity of non-heme diiron(II) complexes with NO in general is quite well-known.[10, 12, 70] A dinitrosyl complex, $[Fe_2(N\text{-Et-HPTB})(PhCOO)(NO)_2](BF_4)_2$ (**4**)[58] (Chart 1) could mediate the photoproduction of N_2O at low temperatures in high yield[71] and formation of a mononitrosyl species was invoked in the mechanism. A functional model complex for FNORs, $[Fe_2(BPMP)(OPr)(NO)_2](BPh_4)_2$ (**5**),[59] (Chart 1) could mediate the reduction of NO to N_2O with quantitative yield upon chemical as well as electrochemical reduction. It was further shown with the triflate analogue of **5** that one equivalent of

reducing agent is in fact sufficient for the quantitative generation of N_2O.[53] However, the dinitrosyl diiron(II) complex, $[L\{Fe(NO)\}_2(\mu\text{-OAc})](ClO_4)_2$ (**6**)[72] (where L is a dinucleating pyrazolate/triazacyclononane hybrid ligand) displays an anti orientation of the $\{FeNO\}^7$ units compared with the syn orientation in **4**[58] and **5**[59] and is unable to produce N_2O upon reduction. Very recently, a nonheme diiron model complex has been shown (by N.L.) to be capable of directly reducing NO to N_2O in quantitative yield without the use of an external reductant.[57] However, despite multiple reports available in the literature regarding reduction of NO to N_2O by diiron complexes in relation with FNORs, the fate of the iron complexes after N_2O generation remained elusive. Along those lines, we have reported the sole example of a model mononitrosyl diiron(II) complex, $[Fe_2(N\text{-Et-HPTB})(NO)(DMF)_3](BF_4)_3$ (**1**), which could mediate the reduction of NO to N_2O in ~89% yield upon chemical as well as electrochemical reduction.[55]

With this exciting initial results, we set out to perform a detailed comparative reactivity study for **1** and its dinitrosylated analogue **2** and to find out the exact fate of the nitrosylated species after N_2O generation. Here we report a detailed account for the synthesis, structural and spectroscopic characterization and reactivity of **1**, a dinitrosyl diiron(II) complex, $[Fe_2(N\text{-Et-HPTB})(NO)_2(DMF)_2](BF_4)_3$ (**2**), and a related mixed valent diiron(II, III) complex, $[Fe_2(N\text{-Et-HPTB})(OH)(DMF)_3](BF_4)_3$ (**3**). Complex **2** could mediate the reduction of NO to N_2O upon chemical and electrochemical reduction at RT. Interestingly though, both **1** and **2** were found to produce stoichiometric amounts of N_2O upon addition of 1 eq. of a chemical reductant, while only 50% N_2O was produced by **1** upon use of 0.5 eq. of the reductant. The reactions leading to N_2O generation were studied further by IR and EPR spectroscopy, and mass spectrometry, while the final products obtained after N_2O generation upon one- and two-electron reduction of **2** were unambiguously characterized, for the first time, by single crystal X-ray structure determination. Finally, based on our comparative reactivity studies, spectroscopic investigations, theoretical calculations, and the molecular structure determination of the reaction products, mechanisms for the reduction of NO to N_2O

Chart 1. Abbreviations and designations of compounds

$[Fe_2(N\text{-Et-HPTB})(NO)(DMF)_3](BF_4)_3$	**1**[55]
$[Fe_2(N\text{-Et-HPTB})(NO)_2(DMF)_2](BF_4)_3$	**2**
$[Fe_2(N\text{-Et-HPTB})(OH)(DMF)_3](BF_4)_3$	**3**
$[Fe_2(N\text{-Et-HPTB})(PhCOO)(NO)_2](BF_4)_2$	**4**[58]
$[Fe_2(BPMP)(OPr)(NO)_2](BPh_4)_2$	**5**[59]
$[L\{Fe(NO)\}_2(\mu\text{-OAc})](ClO_4)_2$	**6**[72]
$[Fe_2(N\text{-Et-HPTB})(DMF)_4](BF_4)_3$	**7**[73]
$[Fe_2(N\text{-Et-HPTB})(\mu\text{-SR})(DMF)_n](BF_4)_2$	R = Me, n = 0, **8a**[74]; R = Ph, n = 1, **8b**[74]
$[Fe_2(N\text{-Et-HPTB})(\mu\text{-SCOCH}_3)](BF_4)_2$	**9**[55]
$[Fe_2(N\text{-Et-HPTB})(OH)(NO)(DMF)_2](BF_4)_3$	**10**[75]
$[Fe_4(N\text{-Et-HPTB})_2(\mu\text{-OH})_2(\mu\text{-O})](BF_4)_4$	**11**
$[Fe_4(N\text{-Et-HPTB})_2(\mu\text{-OH})_2](BF_4)_4$	**12**

H*N*-Et-HPTB,[74, 76] (*N*,*N*,*N*′,*N*′-tetrakis(2-(l-ethylbenzimidazolyl))-2-hydroxy-1,3-diaminopropane; HBPMP, [77-78] 2,6-bis[(bis(2-pyridylmethyl)amino)methyl]-4-methylphenol; L is a dinucleating pyrazolate/triazacyclononane hybrid ligand

by **1** and **2** are proposed.

Experimental Section

Preparation of Compounds. All reactions and manipulations were performed under a pure argon atmosphere using either standard Schlenk techniques or an inert atmosphere box. Solvents were dried following standard procedures.[79] Tritylnitrosothiol (Ph_3CSNO)[80-81], $[Fe_2(N\text{-Et-HPTB})(NO)(DMF)_3](BF_4)_3$ (**1**)[55], $[Fe_2(N\text{-Et-HPTB})(DMF)_4](BF_4)_3$ (**7**)[73], $[Fe_2(N\text{-Et-HPTB})(RS)(DMF)_n](BF_4)_2$ (R = Me, n = 0, **8a**; R = Ph, n = 1, **8b**)[74], $[Fe_2(N\text{-Et-HPTB})(\mu\text{–SCOCH}_3)](BF_4)_2$ (**9**)[55] and $[Fe_2(N\text{-Et-HPTB})(OH)(NO)(DMF)_2](BF_4)_3$ (**10**)[75] were prepared following the respective literature procedures. Cobaltocene, thioacetic acid, $(NO)(BF_4)$, $Fe(BF_4)_2\cdot 6H_2O$, $(Cp_2Fe)(BF_4)$, Cp_2Fe, and Et_3N were obtained from commercial sources and were used without further purification. In the preparations that follow, all the filtrations were performed through Celite and solvent removal steps were carried out in vacuo inside an inert (argon gas) atmosphere box. Yields reported in each case are for recrystallized compounds and are averages of individual yields obtained from multiple batches of reactions, calculated using corresponding molecular weights of the compounds shown in Table 1.

*[Fe_2(N-Et-HPTB)$(NO)_2(DMF)_2](BF_4)_3$ (**2**)*. To a solution of **7** (0.04 mmol, 55.44 mg) in 1 mL of DMF was added Ph_3CSNO (0.24 mmol, 73.2 mg) in 1 mL of DMF and the green solution was stirred for 4 hours. The solution was filtered, and Et_2O was allowed to diffuse into the filtrate overnight at −35°C with an additional 1 day standing at r.t. to afford greenish brown colored block shaped diffraction quality crystals. The crystals were washed several times with THF and Et_2O followed by drying under vacuum to yield 34.9 mg (60%) of **2**. The identity of the compound was confirmed by a single crystal X-ray structure determination. Anal. Calcd for: $C_{49}H_{64}B_3F_{12}Fe_2N_{14}O_5 \cdot 0.5(C_3H_7NO)$ (**2**·0.5DMF): C, 45.34%; H, 5.09%; N, 15.18%. Found: C, 45.67%; H, 4.77%; N, 15.26%. ESI-MS in MeCN: found (calcd) for $[Fe_2(N\text{-Et-HPTB})(NO)_2]^{3+}$: m/z 298.78 (298.76). IR: ν_{NO} = 1782 cm^{-1} (KBr pellet); 1798 cm^{-1} (2 mM solution in MeCN); 1789 cm^{-1} (7.7 mM solution in CH_2Cl_2). UV−Vis (0.2 mM in MeCN) λ nm (ε, $M^{-1}cm^{-1}$): 320 (4763±700), 425 nm (1785±160), 510 (558±80), 625 nm (505±70). Mössbauer: δ = 0.64 mm/s (ΔE_Q = 1.33 mm/s).

*Alternative synthesis of **2** from **1***. To a solution of **1** (0.018 mmol, 24 mg) in 1 mL of DMF was added Ph_3CSNO (0.036 mmol, 11 mg) in 0.5 mL of DMF. The reaction mixture was stirred for 2 hours, filtered, and Et_2O was allowed to diffuse into the filtrate overnight at −35°C with an additional 1 day standing at r.t. to afford greenish brown-colored block-shaped diffraction quality crystals. The crystals were washed with Et_2O followed by drying under vacuum to yield 16.5 mg (67%) of **2**. The identity of the compound was confirmed by unit cell determination of the single crystals, and IR spectroscopy.

*Alternative synthesis of **2** from 7 using NO gas*. To a solution of **7** (0.04 mmol, 55.44 mg) in 2 mL of DMF, NO gas was purged for 2 minutes. The solution was filtered, and Et_2O was allowed to diffuse into the filtrate overnight at −35°C with an additional 1 day standing at r.t. to afford greenish brown colored block shaped diffraction quality crystals. The crystals were washed with Et_2O followed by drying under vacuum to yield 33.7 mg (58%) of **2**. The identity of the compound was confirmed by a single crystal X-ray structure determination and IR spectroscopy.

*Alternative synthesis of **2** from **8a** or **8b**.* To a solution of **8a** (0.04 mmol, 42 mg) in 2 mL of MeCN was added Ph_3CSNO (0.08 mmol, 24.4 mg) in 2 mL of THF and the green solution was stirred for 4 hours. The solvent was evaporated to dryness and the solid residue was washed several times with THF. The solid residue obtained was dissolved in DMF, filtered, and Et_2O was allowed to diffuse into the filtrate overnight at −35°C with additional 1 day standing at r.t. to afford greenish brown colored block shaped diffraction quality crystals (16.7 mg, 29%) of **2**. The identity of the compound was confirmed by single crystal X-ray structure determination and IR spectroscopy.

Complex **2** was synthesized from **8b** (0.02 mmol, 22.32 mg) and Ph_3CSNO (0.04 mmol, 12.2 mg) following the same procedure as described above (starting from **8a)**, in 35% (9.56 mg) yield, and the identity of **2** was confirmed by unit cell determination of the single crystals and IR spectroscopy.

*$[Fe_2(N\text{-}Et\text{-}HPTB)(OH)(DMF)_3](BF_4)_3$ (**3**).* To a solution of **9** (0.05 mmol, 54.1 mg) in 2 mL of MeCN was added a solution of ferrocenium tetrafluoroborate (0.11 mmol, 30.02 mg) in 2 mL of MeCN and the resulting solution was stirred for 6 hours. The solvent was evaporated to dryness and the solid residue obtained was washed several times with THF, dissolved in DMF, filtered, and Et_2O was allowed to diffuse into the filtrate overnight at −35°C with additional 1 day standing at r.t. to afford brownish yellow colored diffraction quality crystals (34.5 mg, 49%). The identity of the compound was confirmed by a single crystal X-ray structure determination. Anal. Calcd for: $C_{52}H_{71}B_3F_{12}Fe_2N_{13}O_5 \cdot 0.5(C_4H_{10}O)$ (**3**$\cdot 0.5Et_2O$): C, 47.43%; H, 5.60%; N, 13.32%. Found: C, 47.27%; H, 5.29%; N, 13.20%. UV−Vis (0.2 mM in DMF) λ nm (ε, $M^{-1}cm^{-1}$): 300 (5990±400), 575 (770±15). Mössbauer: $\delta = 1.22$ mm/s ($\Delta E_Q = 3.27$ mm/s, 44.3%), 0.44 mm/s ($\Delta E_Q = 0.79$ mm/s, 55.7%).

*$[Fe_4(N\text{-}Et\text{-}HPTB)_2(\mu\text{-}OH)_2(\mu\text{-}O)](BF_4)_4$ (**11**).* To a solution of **2** (0.02 mmol, 27.5 mg) in 1 mL of CH_2Cl_2 was added a solution of cobaltocene (0.02 mmol, 3.78 mg) in 0.5 mL of CH_2Cl_2. The color of the solution immediately changed from dark green to dark brown. The resulting solution was stirred for 1 hour and evaporated to dryness. The residue obtained was dissolved in 1 mL of DMF, filtered, and Et_2O was

allowed to diffuse into the filtrate overnight at −35°C, followed by letting the solution stand at room temperature for 10 days to yield a mixture of pale yellow-colored needle-shaped and brown coloured block-shaped crystals. The block-shaped crystals were identified as $[Fe_4(N\text{-Et-HPTB})_2(\mu\text{-OH})_2(\mu\text{-O})](BF_4)_4$ (**11**) and the needle-shaped crystals were identified as $Cp_2Co(BF_4)$ by single crystal X-ray structure determination.

*$[Fe_4(N\text{-Et-HPTB})_2(\mu\text{-OH})_2](BF_4)_4$ (**12**).* To a solution of **2** (0.02 mmol, 27.5 mg) in 1 mL of CH_2Cl_2 was added a solution of cobaltocene (0.04 mmol, 7.56 mg) in in 0.5 mL of CH_2Cl_2. The color of the solution immediately changed from dark green to yellowish brown. The resulting solution was stirred for 1 hour and evaporated to dryness. The residue obtained was dissolved in 1 mL of DMF, filtered, and Et_2O was allowed to diffuse into the filtrate overnight at −35°C, followed by letting the solution stand at room temperature for 10 days to yield a mixture of pale yellow-colored needle-shaped and yellowish brown-colored block-shaped crystals. The block-shaped crystals were identified as $[Fe_4(N\text{-Et-HPTB})_2(\mu\text{-OH})_2](BF_4)_4$ (**12**) and the needle-shaped crystals were identified as $Cp_2Co(BF_4)$ by single crystal X-ray structure determination.

Computational Methods. Optimization and frequency calculations on $\mathbf{1}^{3+/2+}$ and $\mathbf{2}^{3+/2+}$ were performed with Gaussian09[82] using the B3LYP functional[83-84] and 6-311G(d) basis set.[85-87] Both of these complexes contain two antiferromagnetically coupled iron centers. These were treated by generating three fragments, one fragment containing the ligand scaffold, and the other two fragments containing one each of the Fe or Fe-NO units. An initial guess was performed first in Gaussian09 by making one of the Fe-containing fragments antiferromagnetically coupled to the other Fe. This guess was then utilized to begin single point and geometry optimization calculations. Once optimized, a frequency calculation was performed, and the final optimized structure was used in a subsequent Orca[88-89] 4.0.1.2 single point calculation to visualize the electronic structure. This single point was performed on the Gaussian09 B3LYP optimized structure (without fragments) utilizing the B3LYP/G functional and 6-311G(d) basis set with the def2/J

auxiliary basis set.[90] The ferromagnetic single point was generally calculated first, and the spins at one of the Fe-NO units were then flipped using the SpinFlip option in order to proceed.

General Physical Methods. Elemental analyses were recorded using a Perkin-Elmer 2400 series II CHNS analyzer. Cyclic voltammetry studies of **2** and **3** (10^{-3} M) in DMF were performed using a CHI620E electrochemical analyzer (CH Instruments, USA). A three-electrode setup was employed comprising a glassy carbon working electrode, a platinum wire auxiliary electrode, and a silver wire as the pseudo-reference electrode. Tetra-n-butylammonium hexafluorophosphate (0.1 M) was used as the supporting electrolyte. Electrochemical potentials are referenced internally to the ferrocene/ferrocenium couple at 0.0 V. Electronic absorption spectra were recorded using a Cary 60 UV-Vis spectrophotometer. IR spectra of the solid samples as KBr pellets were recorded using a Perkin Elmer Spectrum BX FT-IR. The solution FT-IR data were measured on a Perkin Elmer FT-IR spectrometer (Frontier) instrument. Mössbauer spectra were recorded using an alternating constant *WissEl* Mössbauer spectrometer, consisting of an MR 360 Drive Unit, an MV-1000 velocity transducer, and an LND 45431 proportional counter mounted on an LINOS precision bench. The system was operated in a horizontal transmission geometry with source, absorber, and detector in a linear arrangement. The temperature was controlled and maintained using a Janis SHI closed-cycle helium cryostat. Measurements were performed at 80 K. Data acquisition was performed using a 512 channel analyzer. Isomer shifts were referenced versus α-iron metal foil at ambient temperatures. The simulation of experimental data was performed using the *Mfit* program. Magnetic susceptibility measurements were conducted on a Quantum-Design MPMS XL-5 SQUID magnetometer, equipped with a 5 T magnet. Powder samples were loaded into a Teflon bucket (for **1**) or into a gelatin capsule (with addition of a polyfluorinated oil to prevent crystal orientation, for **2**) and placed in a plastic straw. The raw data were corrected for the diamagnetic contribution of the sample holder (and of the oil in case of **2**) as well as the diamagnetic contribution of the complexes using $\chi_M^{dia}(\text{sample}) = -0.5 \cdot M \cdot 10^{-6}$

$cm^3 \cdot mol^{-1}$. The data were fit with the *julX* program[88] using the appropriate Heisenberg-Dirac-van-Vleck (HDvV) spin Hamiltonian for isotropic exchange coupling and Zeeman splitting, equation (1).

$$\hat{H} = -2J\hat{S}_1\hat{S}_2 + g\mu_B\vec{B}(\vec{S}_1 + \vec{S}_2) \quad (1)$$

EPR spectra were recorded using a Bruker X-band EMX spectrometer equipped with an Oxford liquid helium cryostat. Spectra were recorded on ~2mM frozen solutions using 20mW microwave power and 100kHz field modulation at a 5G amplitude. IR spectroelectrochemistry experiments were performed using a LabOmak UF-SEC thin layer cell, with Pt mesh working and counter electrodes, and an Ag wire pseudo-reference electrode.

N_2O yield Calculation. X μmol (X = 9.6, 5.2) of **2** were dissolved in 2 mL of CH_2Cl_2 in a septum sealed 25 mL round bottom flask with a 14/20 joint. 1 or 2 equivalents of $CoCp_2$ (with respect to the concentration of **2**) were dissolved in 0.5 mL of CH_2Cl_2 and the solution was syringed into the flask. The resulting solution was stirred for ~5 min prior to evacuating the headspace of the flask via cannula transfer to an evacuated Pike HT gas-IR cell (190 milli-torr) for exactly 20 s. After subtraction of a CH_2Cl_2 blank taken under the exact same conditions, the IR spectrum was converted to absorbance and the N-N stretch of N_2O was integrated using a straight-line baseline correction from 2150-2275 cm^{-1}. The integration was then compared to a standard curve.[53]

X-ray Structure Determinations. The molecular structures of compounds **2**, **3**, **11** and **12** were determined by single crystal X-ray structure determinations. Diffraction-quality crystals were obtained as described in the synthesis parts of the respective compounds above. Single crystals were coated with Parabar oil and were mounted under a nitrogen cold stream. Data collections were performed either at 150 K (**2**, **3**) on a Bruker SMART APEX II diffractometer with graphite–monochromated Mo Kα radiation (λ = 0.71073 Å) controlled by the APEX II (v. 2010.1-2) software package or at 100 K (**11** and **12**) on a Bruker D8VENTURE Microfocus diffractometer equipped with PHOTON II Detector, with Mo Kα radiation (λ = 0.710 73 Å), controlled by the APEX III (v2017.3−0) software package. The raw data were integrated and corrected for Lorentz and polarization effects with the aid of the Bruker APEX II[34]/APEX

Table 1. X-ray crystallographic data for compounds **2**, **3**, **11** and **12**[a]

compounds	**2**·DMF	**3**·DMF	**11**	**12**·6DMF
CCDC numbers	1892324	1770560	1892326	1892325
Temp. (K)	150	150	100	100
formula	$C_{52}H_{70}B_3F_{12}Fe_2N_{15}O_6$	$C_{55}H_{78}B_3F_{12}Fe_2N_{14}O_6$	$C_{86}H_{100}B_4F_{16}Fe_4N_{20}O_5$	$C_{104}H_{142}B_4F_{16}Fe_4N_{26}O_{10}$
formula weight	1373.36	1403.44	2064.49	2487.07
crystal system	triclinic	triclinic	triclinic	orthorhombic
space group	$P\bar{1}$	$P\bar{1}$	$P\bar{1}$	$Pna2_1$
a, Å	13.0940(19)	11.489(4)	18.424(6)	29.597(3)
b, Å	13.229(2)	16.691(6)	18.600(6)	14.1253(12)
c, Å	21.320(3)	17.688(6)	21.629(6)	29.688(3)
α, deg	79.228(4)	85.673(5)	113.567(7)	90
β, deg	80.542(4)	84.727(5)	90.687(8)	90
γ, deg	66.249(4)	69.969(4)	116.641(8)	90
V, Å^3	3304.4(9)	3169.8(18)	5905(3)	12411.6(18)
Z	2	2	2	4
ρ_{calcd}, gm/cm^3	1.380	1.470	1.161	1.331
μ, mm^{-1}	0.530	0.553	0.556	0.546
θ range, deg	0.977-25.882	1.157-25.568	2.099-25.774	2.106-25.714
completeness to θ, %	99.4	98.9	93.8	99.7
reflections collected	34519	31956	52982	133860
independent reflections	12744	11764	21259	23091
R(int)	0.1256	0.0989	0.1240	0.0897
restraints[b]	184	17	47	103
parameters	762	791	1148	1471
Max., min. transmission	0.7453, 0.6608	0.7453, 0.5911	0.7452, 0.6071	0.7453, 0.6714
R1[c](wR2)[d] [I>2sigma(I)]	0.0967 (0.2368)	0.0786 (0.1833)	0.1606 (0.4090)	0.0596 (0.1446)
R1[c](wR2)[c]	0.2176 (0.3057)	0.1519 (0.2247)	0.2657 (0.4750)	0.0850 (0.1645)
GOF(F^2)[e]	1.010	1.024	1.317	1.023
[f]max, min peaks, e.Å^{-3}	0.665, -0.701	1.020, -0.980	2.480, -0.935	0.888, -0.867

[a]Mo Kα radiation (λ = 0.71073 Å). [b] **2**·DMF, disordered ligand and three BF_4^-; **3**·DMF, disordered DMF and three BF_4^-; **11**, disordered ligand and four BF_4^-; **12**·6DMF, disordered DMF and two BF_4^-; [c]R1 = $\Sigma||F_o|-|F_c||/\Sigma|F_o|$. [c]wR2 = $\{\Sigma[w(F_o^2-F_c^2)^2]/\Sigma[w(F_o^2)^2]\}^{1/2}$. [e]GOF = $\{\Sigma[w(F_o^2-F_c^2)^2]/(n-p)\}^{1/2}$, where n is the number of data and p is the number of refined parameters. [f] electron density near: **2**·DMF, disordered BF_4^-; **3**·DMF, disordered BF_4^-; **11**, at 1.20Å from Fe3; **12**·6DMF, disordered BF_4^-.

III program suite. Absorption corrections were performed by using SADABS. Space groups were assigned by considering the systematic absences (determined by XPREP) and analysis of metric symmetry. Space

groups were further checked by PLATON[91-92] for additional symmetry. Structures were solved by direct methods and refined against all data in the reported 2θ ranges by full-matrix least squares refinement on F^2 using the SHELXL program suite[93] and the OLEX 2[94] interface. Hydrogen atoms at idealized positions were included in the final refinements. The OLEX 2 interface was also used for structure visualization and for drawing ORTEP[95-96] plots. Crystallographic data and final agreement factors are provided in Table 1. The individual CIFs include the refinement details and explanations (wherever applicable). Complexes **11** and **12** represent two elusive end products after N_2O generation from a dinitrosyl diiron(II) complex upon addition of 1 and 2 equivalents of reductants, respectively and could never be identified previously. Data quality of **11** was, however, poor and hence a final R value lower than 10 could not be obtained. The molecular structure and the cif of **11** is nonetheless included in this report, since the molecular structure is otherwise clean, compliments the formation of **12** and for the first time clearly shows the nature of the end product after semireduction of **2** by cobaltocene.

RESULTS AND DISCUSSION

Synthesis. Synthesis of a pure mononitrosyl diiron(II) complex in a symmetric dinucleating ligand platform is generally thwarted by (i) lack of selectivity, and (ii) possible scrambling and dissociation of NO.[10] A previously reported diiron(II) complex, $[Fe_2(N\text{-Et-HPTB})(NO)_{0.6}(DMF)_{3.4}](BF_4)_3$, was described as a mixture of ~60% $[Fe^{II}\{FeNO\}^7]$ species and ~40% Fe^{II}_2 species on the basis of single crystal X-ray structure determination and Mössbauer spectroscopy[75] and therefore may not be considered as a suitable candidate for a further structure-function study. Controlled experiments for studying stepwise addition of NO also did not show the preferential formation of a mononitrosyl complex but straight-forward formation of the dinitrosyl complex.[59] Considering these facts, we set out to find an effective synthetic strategy for the elusive mononitrosyl diiron(II) complex, using redox reactions with $[Fe_2(N\text{-Et-HPTB})(RS)(DMF)_n](BF_4)_2$ (R = Me, n = 0, **8a**; R = Ph, n = 1, **8b**)[74] and **9**[55] (Chart 1) as the starting materials. The mononitrosyl diiron(II) complex, **1**,[55] has been reported by us recently, and the full

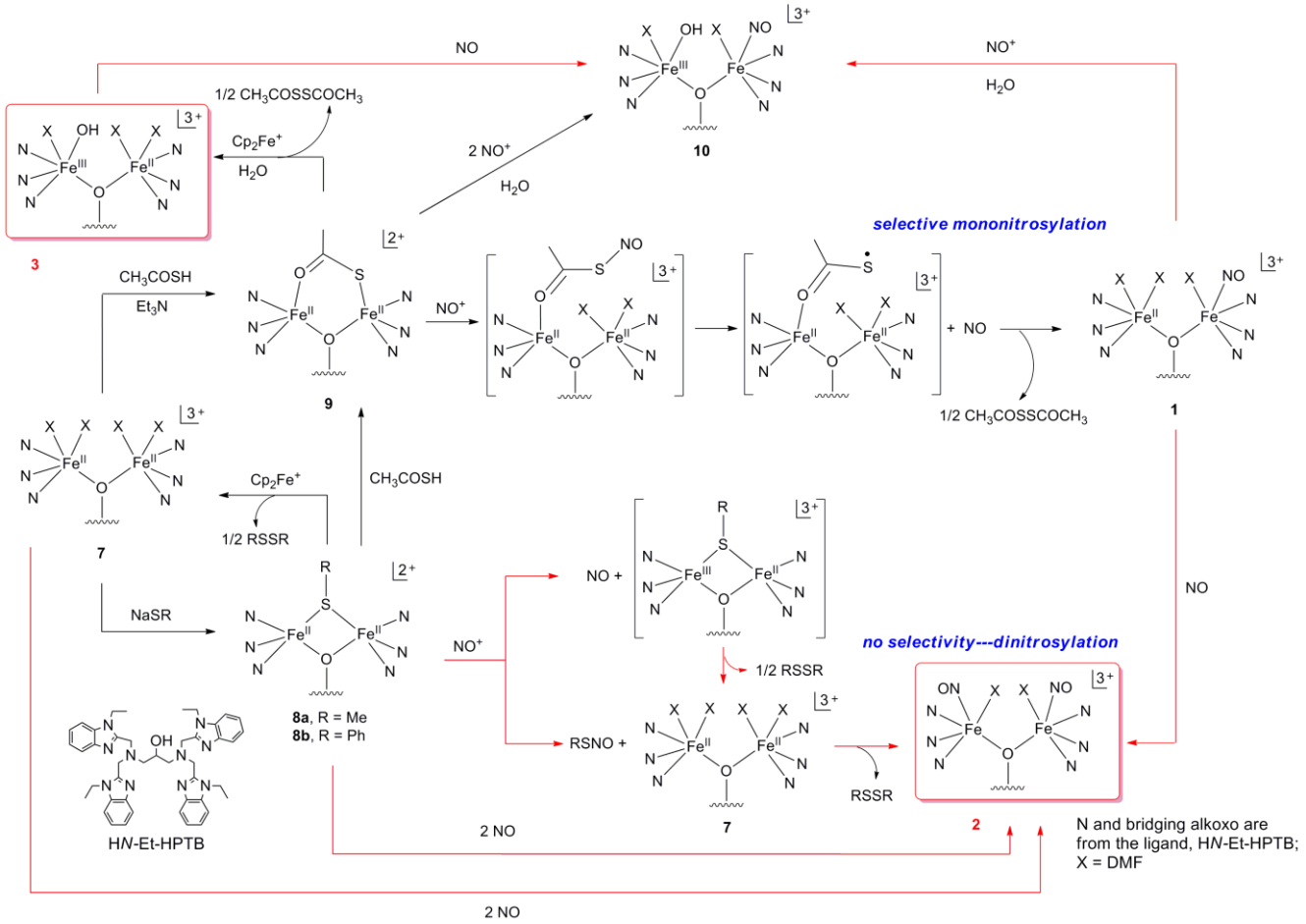

Scheme 1. Schematic presentation of the synthesis and reactivity of **1**–**3**. Ph_3CSNO and $(NO)(BF_4)$ were used as the sources of NO and NO^+, respectively. Possible reaction intermediates (not isolated) are shown in brackets. The new complexes, **2** and **3**, and the new reactions are marked with red color. Complexes **1**; **9**;[55] **7**;[73] **8a**, **8b**;[74] and **10**[75] have been reported previously.

synthetic details and the synthetic rationale for this family of compounds are provided here. The complete synthetic scheme for **1-3** and their chemical interconversions with other related complexes (**7-10**) are summarized in Scheme 1. Complex **9** could be synthesized[55] either by the reaction of $[Fe_2(N\text{-Et-HPTB})(DMF)_4](BF_4)_3$ (**7**)[73] with CH_3COSH/Et_3N or by the reaction of **8a**/**8b**[74] with CH_3COSH (Scheme 1). Upon treatment with one equivalent of $(NO)(BF_4)$, **8a** and **8b** yielded a mixture of the dinitrosyl diiron(II) compound **2** and the diferrous complex **7**. The mechanism for this reaction may involve the initial formation of a thiolate bridged $Fe^{II}Fe^{III}$ species which may be reduced by the bridged thiolate to

form one equivalent of **7** and NO each, followed by nitrosylation of **7** in a non-selective manner (Scheme 1) to yield **2**. Such a possibility has already been substantiated by one of us (A.M.) for the reaction between **8b** and $(Cp_2Fe)(BF_4)$.[74] Alternatively, the bridged thiolate may react directly with NO^+ to generate **7** and the corresponding RSNO (R = Me, Ph)[97-98] followed by the nitrosylation of **7** by the RSNO, again in a non-selective manner, to yield half equivalents of **2** and the corresponding RSSR. Compound **2**, however, may be obtained as an analytically pure product by the reaction between 2 eq. of tritylnitrosothiol (Ph_3CSNO)[80-81] and either **7** (60% yield) or **8a** (29% yield) or **8b** (35% yield). In practice, 4-6 eq. of Ph_3CSNO are actually used in order to counter the possible dissociation of NO and incomplete nitrosylation. Alternatively, **2** could also be synthesized in 58% yield by the treatment of **7** with excess NO gas.

However, unlike the formation of **7** from **8a**/**8b**, reaction of **9** with $(Cp_2Fe)(BF_4)$ in a 1:1 ratio yielded a mixed-valent $Fe^{II}Fe^{III}$ compound, **3**, along with $CH_3COSSCOCH_3$ (Figure S1) and **9**. The hydroxyl group in **3** might have originated from the starting material, **9**, which in turn was made from $Fe(BF_4)_2{\cdot}6H_2O$, and/or from moisture in the solvents. A similar situation was reported previously for the origination of the hydroxyl group in **10**.[75] This result indicates that the mixed-valent species that may have been generated from **9** (for **9**, E_{pa} = 0.15 V, 0.77 V vs. Cp_2Fe^+/Cp_2Fe) is incapable of oxidizing the bridging thioacetate ($E_{1/2}$ for $CH_3COS^{\bullet}/CH_3COS^-$ = 0.58 V vs. Cp_2Fe/Cp_2Fe^+ in water)[99] to its disulfide form along with the formation of **7**. Also, because of the high reduction potentials, the iron centers in **9** may not be oxidized by $(Cp_2Fe)(BF_4)$. Rather, the bridged thioacetate may be oxidized directly[100] by Cp_2Fe^+ to yield a mixture of $CH_3COSSCOCH_3$, **7**, and **3**. Here, **3** may be formed via the one electron oxidation of the solvent coordinated diiron(II) complex, identical or similar with **7**, which may be generated after oxidation of the bridging thioacetate to the corresponding disulfide. Indeed, the use of two equivalents of $(Cp_2Fe)(BF_4)$ in this reaction yielded **3** as the sole iron complex in 49% yield, while the yield of $CH_3COSSCOCH_3$ was found to be ~33% from ^1H NMR spectroscopic measurements. Inspired by these

results, the reaction of **9** with (NO)(BF_4) was then carried out, which ultimately yielded the desired mononitrosyl diiron(II) complex, **1** as a crystalline solid in 50% yield.[55] Upon treatment of (NO)(BF_4), the bridged thioacetate in **7** may form CH_3COSNO[97-98] which in turn will undergo homolytic cleavage to generate NO and $CH_3COS^{\bullet}$ (Scheme 1). Unlike the weak bridging capacity of RSNO and $RS^{\bullet}$, both CH_3COSNO and $CH_3COS^{\bullet}$ may still remain bound to one of the two iron(II) centers via the oxygen atom and hence, two different coordination environments for the two iron(II) centers are maintained during the course of the reaction (Scheme 1). This asymmetry in the coordination sphere of the iron(II) centers along with the controlled release of NO in solution might have favored the selective formation of **1** along with $(CH_3COS)_2$ (average yield = 39%).[55] While a diiron(II,III) species may also form during the reaction of **9** with NO^+, the bridged thioacetate, owing to its high reduction potential, may not be oxidized by the diiron(II,III) species to generate **7** and thus, the possible formation of a dinitrosyl complex during the reaction is thwarted. The stability of **1** and **2** in solution up to at least 2 days was confirmed by IR and UV-Vis spectroscopy, elemental analysis and unit cell determination of the single crystals obtained after recrystallization. In contrast with [Fe_2(*N*-Et-HPTB)(PhCOO)](BF_4)$_2$[73, 101], **9** did not react at all with Ph_3CSNO. Since the $\{FeNO\}^7$ unit is best described as (Fe^{III})(NO^-),[44-45, 49, 51] the reluctance of **9** to yield nitrosylated products may be due to the much higher reduction potential of the iron(II) centers in **9** (E_{pa} = 0.15 V, 0.77 V) compared to that observed in the case of [Fe_2(*N*-Et-HPTB)(PhCOO)](BF_4)$_2$ ($E_{1/2}$ = −0.18 V, 0.36 V).[73] While reaction of **1** with Ph_3CSNO yielded the dinitrosyl complex, **2**, in 67% yield, treatment of **1** with 1 eq. (NO)(BF_4) converted **1** to a previously reported compound, [Fe_2(*N*-Et-HPTB)(OH)(NO)(DMF)$_2$](BF_4)$_3$ (**10**)[75]. Complex **10** may also be obtained by nitrosylation of **3** (Scheme 1). Both of these transformations were confirmed by single crystal X-ray structure determinations of the products. Compound **10**[75] exhibits a [$\{FeNO\}^7\{Fe^{III}(OH)\}$] formulation and has been recently reported to be an unsuitable candidate for mediating the photoproduction of NO to N_2O.[71] Therefore, it becomes

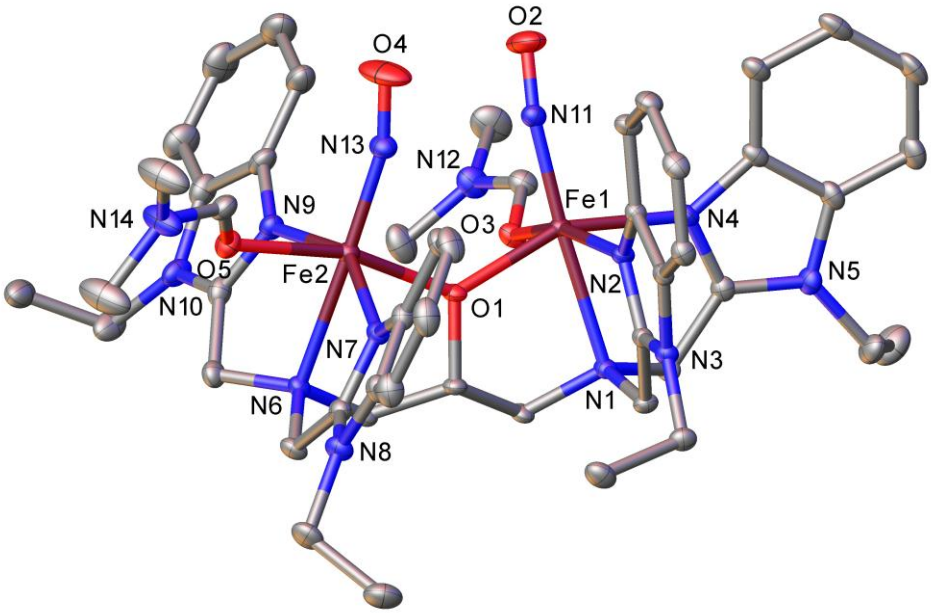

Figure 1. Molecular structure of **2** with 30% probability thermal ellipsoids and partial atom labeling scheme shown. Hydrogen atoms are omitted for clarity.

apparent that a controlled and slow addition of only 1 eq. of (NO)(BF_4) during the selective synthesis of **1** is very crucial. Moreover, addition of 1.1 eq. of (NO)(BF_4) or addition of even 1 eq. of (NO)(BF_4) all at once (instead of slow addition) into the reaction solution has been shown to yield a mixture of **1** (block shaped crystals) and **10** (needle shaped crystals) which may be identified easily by unit cell determinations of the single crystals and the cyclic voltammetry study of the bulk reaction products.

Molecular Structures. Structural characterization of **2** revealed two iron(II) centers in pseudo-octahedral geometry, where each iron(II) center is coordinated by one NO and one DMF molecule (Figure 1). The coordinated DMF molecules are orthogonal to each other. Hexa-coordination for both of the iron(II) centers is satisfied by four coordination sites from the deprotonated ligand, *N*-Et-HPTB^{1-}, to enforce pseudo-octahedral geometries around both of the iron(II) centers in **2**. Compound **2** (Figure 1) shows Fe–NO distances of 1.729 (7) and 1.748(7) Å, N–O distances of 1.123(8) and 1.147(8) Å, and Fe–N–O angles of 174.9(8) and 164.9(7)°, respectively. These metric parameters of **2** are consistent with **1**[55]

Table 2. Selected bond distances, angles and ν_{NO} of nitrosylated complexes.

complexes	Fe–N_{NO} (Å)	N-O (Å)	<Fe-N-O (°)	ν_{NO} (cm^{-1}) (as KBr pellet)
[a]**1**[55]	1.769(7)	1.164(9)	154.9(7)	1768
2	1.748(7)	1.147(8)	164.9(7)	1782
	1.729(7)	1.123(8)	174.9(8)	
4[58]	1.749(8)	1.151(8)	166.6(7)	1785
	1.750(7)	1.156(8)	168.3(7)	
5[59]	1.774(2)	1.156(3)	155.5	1760
	1.796(3)	1.172(3)	144.7	
[b]**6**[72]	1.768	1.143	151	1745
[c]**10**[75]	1.787(2)	1.110(4)	171.0(3)	1792

Molecular structures obtained from multiple batches of single crystals displayed slightly different bond distances and angles for **1**[55] and **10**.[75] Distances and angles are shown for [a]"mononitrosyl 1" in Table S2 of ref. 21, [b]average values for all four Fe(NO)}^{7} units in the asymmetric unit of "**2b**" in ref. 23, and [c]those for "**4a**" in Table 1 of ref. 26.

and the previously reported dinitrosyl complexes, **4**,[58] **5**[59] and **6**[72] (Table 2). Complex **3** contains two iron centers in pseudo-octahedral geometry and shows bond distances of Fe1–$O_{N\text{-Et-HPTB}}$ = 1.950 Å, Fe2–$O_{N\text{-Et-HPTB}}$ = 2.051 Å and Fe1–O2(OH) = 1.860 Å in **3**, similar to previously reported {$Fe^{II}Fe^{III}$–OH} units.[75]

Spectroscopic Characterizations. The electronic absorption spectrum of **2** consists of four distinct transitions (Figure 2) and is in agreement with the absorption spectroscopic features associated with non-heme {FeNO}^{7} complexes.[12, 55, 58] A broad feature centered at 625 nm (ε = 505±70 $M^{-1}cm^{-1}$) is attributed to a d–d transition, while a second band appears as a shoulder at 510 nm (ε = 558±80 $M^{-1}cm^{-1}$). Complex **2** exhibits an additional shoulder at 425 nm (ε = 1785±160 $M^{-1}cm^{-1}$) and an underlying tail from the UV band at 320 nm (ε = 4763±700 $M^{-1}cm^{-1}$). The bands ranging from 320–510 nm are attributed to $NO^-(\pi^*)$ to Fe^{III} charge transfer transitions in non-heme {FeNO}^{7} complexes.[12, 102] The ν_{NO} value of 1782 cm^{-1} (as KBr pellet, Figure S2) in the case of **2** conforms to the typical NO stretching frequencies for

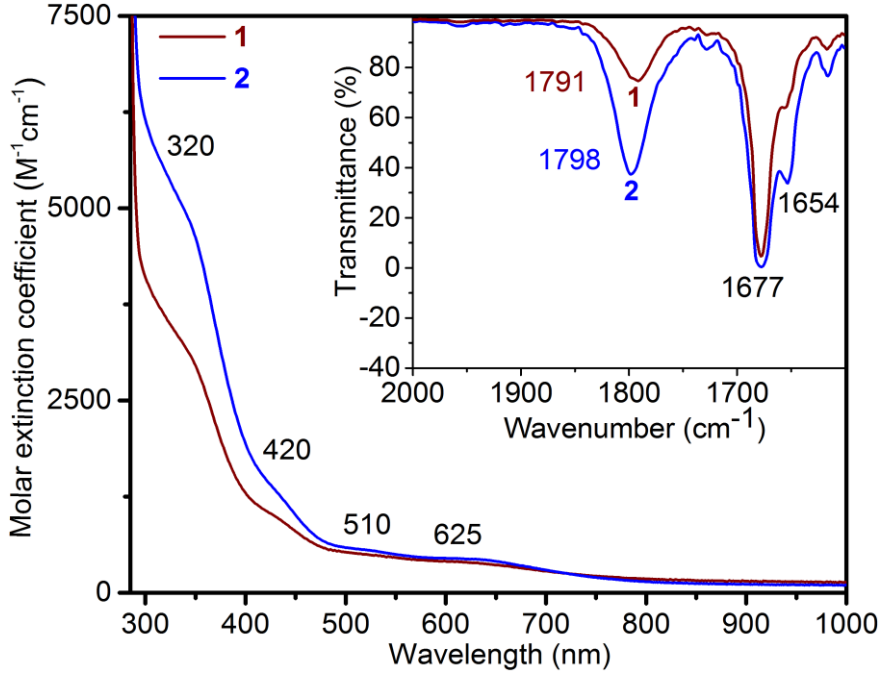

Figure 2. Electronic absorption and IR spectra of **1** and **2** in MeCN. [**1**] = [**2**] = 0.2 mM (UV-Vis) and 2 mM (IR).

high-spin non-heme $\{FeNO\}^7$ complexes[12] and are within the range of 1720-1800 cm^{-1} typically observed for these types of complexes[51] (Table 2). The solution IR spectrum of **2** in MeCN is provided in Figure 2 (inset), which shows the nitrosyl stretching frequency at 1798 cm^{-1}, while the amide-like vibrations from metal-coordinated DMF and free DMF in MeCN[55, 71] are observed at 1653 and 1677 cm^{-1}, respectively. Moreover, upon isotopic substitution of coordinated NO in **2** with ^{15}NO, the nitrosyl stretching frequency shifts from 1783 cm^{-1} to 1762 cm^{-1} in CH_2Cl_2 (Figure S3), thus confirming the assignment of ν_{NO} in **2**.

The Mössbauer spectrum of **2** features only one quadrupole doublet with an isomer shift, $\delta = 0.64$ mm/s (Figure 3), that corresponds to an $\{FeNO\}^7$ dimer. Similar isomer shifts have been reported for other diiron(II) complexes which feature one or more $\{FeNO\}^7$ units.[55, 58, 72, 75] Complex **2** was also found to be EPR silent as expected from the antiferromagnetic coupling of two $S = 3/2$ $\{FeNO\}^7$ units. SQUID magnetometry measurements of **1** and **2** (Figure 4) reveal a weak antiferromagnetic coupling of −11.7 cm^{-1} between $S_1 = 3/2$ and $S_2 = 2$ sites for **1**, which increases to −28.3 cm^{-1} for the two $S = 3/2$ sites in **2**.

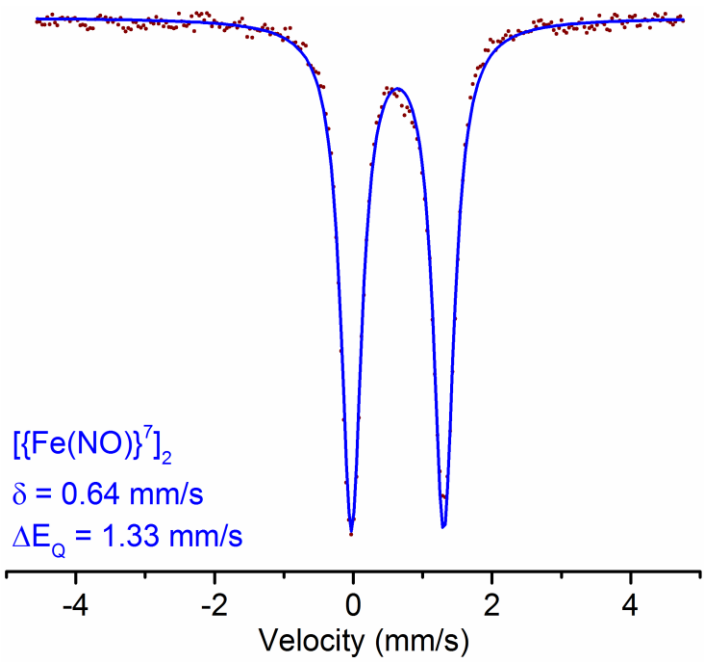

Figure 3. ^{57}Fe Mössbauer spectrum of a polycrystalline sample of **2** at 80K.

This reflects a high-spin ferrous character of the DMF ligated iron ion in **1** and its partial oxidation upon NO binding that gives rise to a Fe^{III}-NO^{-} electronic structure. Mass spectrometry of **2** in MeCN shows the molecular ion peak for **2** at m/z = 298.70 (calcd m/z = 298.76) for $[Fe_2(N\text{-Et-HPTB})(NO)_2]^{3+}$ (Figure S5), while in the case of **1**, the molecular ion peak was observed at m/z = 313.12 (calcd m/z = 313.11) for $[Fe_2(N\text{-Et-HPTB})(NO)(DMF)]^{3+}$ (Figure S6). Together, the single crystal X-ray structure determination, mass spectrometry, SQUID magnetometry and electronic absorption, IR, Mössbauer and EPR spectroscopic measurements thus confirm the formulation of **2** as a $[\{FeNO\}^7]_2$ species, which directly models the dinitrosyl intermediate observed in the catalytic cycle of FNORs. The electronic absorption spectrum of **3** (Figure S4b) shows a band at 575 nm (ε = 770±15 $M^{-1}cm^{-1}$) which may originate either from an alkoxide to Fe(III) charge transfer or an intervalence charge transfer transition and is consistent with the $Fe^{II}Fe^{III}$ formulation. The Mössbauer spectrum of **3** (Figure S4c) features two quadrupole doublets with isomer shifts, δ = 1.22 and 0.44 mm/s, corresponding to the high-spin Fe(II)and Fe(III)

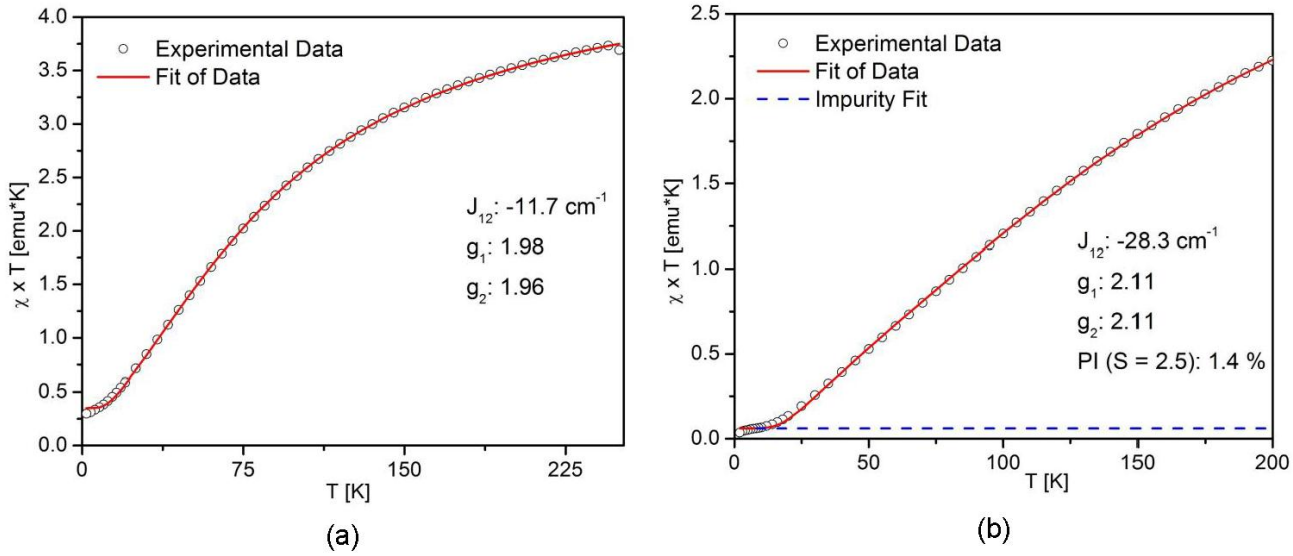

Figure 4. SQUID magnetometry measurements of **1** (a) and **2** (b). The solid red lines represent the best fits using $S_1 = 3/2$ and $S_2 = 2$ for **1** and $S_1 = S_2 = 3/2$ for **2** (see text).

sites, respectively, and is consistent with a high spin mixed-valent {Fe(II)Fe(III)} formulation. Similar Mössbauer parameters have been reported previously for other nonheme diiron(II,III) complexes.[73, 103-106] The observation of discrete quadrupole doublets for **3** at 80 K indicates that the intervalence electron transfer is slow on the Mössbauer time scale ($10^7 s^{-1}$) at 80 K, which is similar to the situation reported for the mixed-valent complexes $[Fe^{II}Fe^{III}(BPMP)(OPr)_2](BPh_4)_2$[103] and $[Fe_2(N\text{-Et-HPTB})(\mu\text{-PhCOO})(DMF)_2](BF_4)_3$.[73] The mixed-valent nature of **3** was also revealed in the EPR spectroscopic measurements. Under the weak field approximation, most mixed-valent diiron(II,III) compounds[73, 77, 104, 106-109] in a low symmetry ligand field exhibit signals with $\langle g_{av} \rangle$ less than 2, characteristic of an S = 1/2 system that results from antiferromagnetic coupling of a high-spin iron(III) ion (S = 5/2) with a high-spin iron(II) ion (S = 2). Complex **3** displays an EPR signal with g ~ 1.857 at 4 K (Figure S4d) and is therefore consistent with a $[Fe^{II}Fe^{III}]$ formulation for **3**. Similar EPR spectra have been reported for other mixed-valent diiron(II,III) complexes with the H*N*-Et-HPTB ligand.[73, 106]

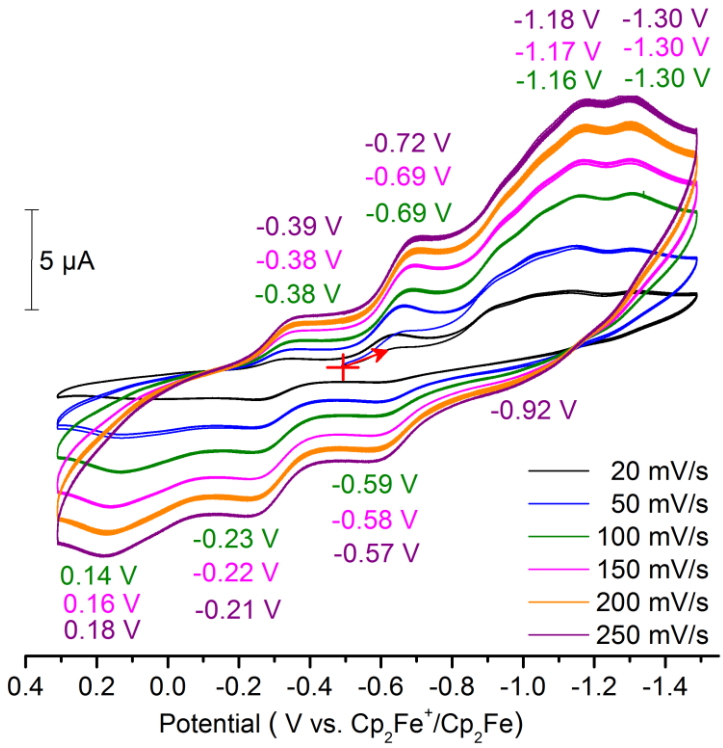

Figure 5. Cyclic voltammetry traces for **2** (multiple scans for each of the six different scan rates are shown) in DMF.

Cyclic Voltammetry and Redox Reactions. Unlike a single irreversible reduction at −1.1 V in the case of the dinitrosyl complex **5**[59], **2** shows two consecutive irreversible reductions at −1.18 and −1.30 V (Figure 5) with a current ratio almost equal to unity (0.98) These two redox events in turn generate a new oxidation wave at −0.57 V in the return scan. Based on the absence of this oxidation event at −0.57 V while scanning in the potential range of −0.5 to −0.95 V (Figure S7), the new oxidation event at −0.57 V may be attributed to oxidation of the reaction product resulting from reduction of **2**, presumably a Fe^{II}–O–Fe^{II} species,[59] or a Fe^{II}–OH–Fe^{II} species that may form after denitrosylation of **2** to generate N_2O. The new reduction event at −0.72 V may then be related to the reduction of the now oxidized reaction product. A single, irreversible, two-electron reduction event at −1.15 V was observed in the cyclic voltammogram of **5**, which was initially assigned to the simultaneous reduction of the two $\{FeNO\}^7$ units in **5**.[59] However, it was established later that this two-electron reduction event was essentially a combination of a one-electron reduction of the dinitrosyl complex, followed by fast N_2O formation, followed by a one-electron

reduction (at about the same potential) of the mixed-valent $Fe^{II}Fe^{III}$ product generated after N_2O release.[53] A similar situation may be expected to be operative in complex **2** as well. Two additional and consecutive oxidation processes at −0.21 V and 0.18 V in the case of **2** are due to the oxidation of the two iron centers of the two $\{FeNO\}^7$ units. The first quasi reversible oxidation at $E_{1/2}$ = −0.30 V (E_{Pa}= −0.21 V, ΔE_V = 180 mV) in the case of **2** may be accessed, in principle, to get the one electron oxidized version of **2**. Complex **2** was therefore allowed to react with 1 eq. of $(Cp_2Fe)(BF_4)$ and the product obtained was characterized as the previously reported compound, $[Fe_2(N\text{-Et-HPTB})(OH)(NO)(DMF)_2](BF_4)_3$ (**10**),[75] which exhibits a $[\{FeNO\}^7\{Fe^{III}(OH)\}]$ formulation. The mixed-valent compound, **3**, showed only one oxidation at 0.82 V due to the $Fe^{II}Fe^{III}/Fe^{III}Fe^{III}$ redox event in the anodic scan, while on the reverse scan (after the reduction event at −0.66 V) a new irreversible oxidation was observed at −0.04 V due to the $Fe^{II}Fe^{II}/Fe^{II}Fe^{III}$ redox event (Figure S4e).

N_2O Generation by 1 and 2. Complex **1** had previously been shown by us to produce N_2O upon electrochemical reduction as well as upon chemical reduction using 1 eq. Cp_2Co with ~ 89% yield.[55] Similar to **1**, complex **2** also does not produce N_2O in solution in the absence of a reductant, and hence may be considered to be in agreement with the inefficiencies of **4**,[58] **5**[59] and the dinitrosyl adducts of ribonucleotide reductase and methane monooxygenase towards reduction of NO to N_2O.[12] Interestingly, **2** could produce N_2O upon electrochemical reduction as well as upon reduction by cobaltocene at room temperature. The generation of N_2O upon electrochemical reduction of **2** was confirmed by IR spectroelectrochemistry experiments (Figure 6a), which show N_2O formation (ν_{N2O} = 2223 cm^{-1}) without any detectable intermediates. The ^{15}NO labeled dinitrosyl complex, **2(^{15}NO)** (ν_{NO} = 1762 cm^{-1}, Figure S3) was prepared by bubbling of ^{15}NO gas into a CH_2Cl_2 solution of **7**. The corresponding IR spectroelectrochemistry experiments showing the formation of $^{15}N_2O$ (ν_{N2O} = 2154 cm^{-1}) upon reduction of the corresponding, isotopically labeled version of **2** are depicted in Figure 6b. Rapid production of N_2O was further confirmed by IR spectroscopic analysis of the reaction headspace upon reduction of complex

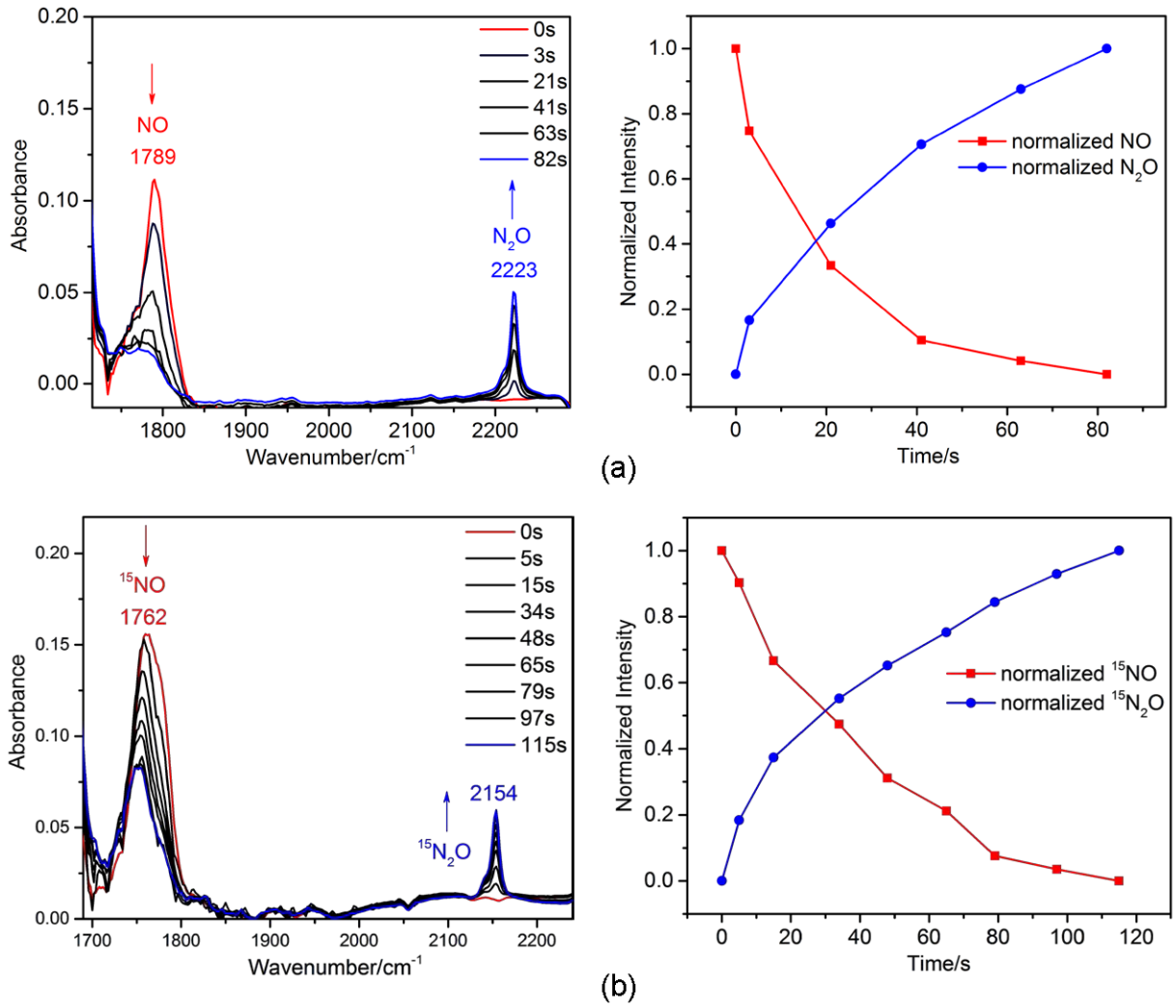

Figure 6. Generation of N_2O upon electrochemical reduction of **2** (a) and **2(**^{15}**NO)** (b).Conditions: [**2**] = 7.7 mM; [**2(**^{15}**NO)**] = 11.4 mM; hold potential at −1.6 V vs Ag wire; CH_2Cl_2, 0.1 M $(Et_4N)(BF_4)$.

2 by 2 equiv of cobaltocene. Integration of the N–N stretching band of N_2O against a calibration curve generated from known N_2O gas standards revealed ~96% yield of N_2O (based on the conc. of **2**) within ~5 min after addition of 2 eq. of cobaltocene (Cp_2Co) as the reductant (Figure S8). Interestingly, it was observed that even 1 eq. of cobaltocene was sufficient for the production of N_2O from **2** with ~ 89% yield (Figure S9). In contrast, while chemical reduction of complex **1** using 1 eq. Cp_2Co could produce N_2O in ~89% yield,[55] use of only 0.5 eq. of Cp_2Co was found to only generate about ~50% of N_2O (relative to the maximum amount of N_2O that can be produced, Figure S10). These results indicate an interesting difference between **1** and **2**: whereas the mononitrosyl diiron(II) complex uses an intermolecular

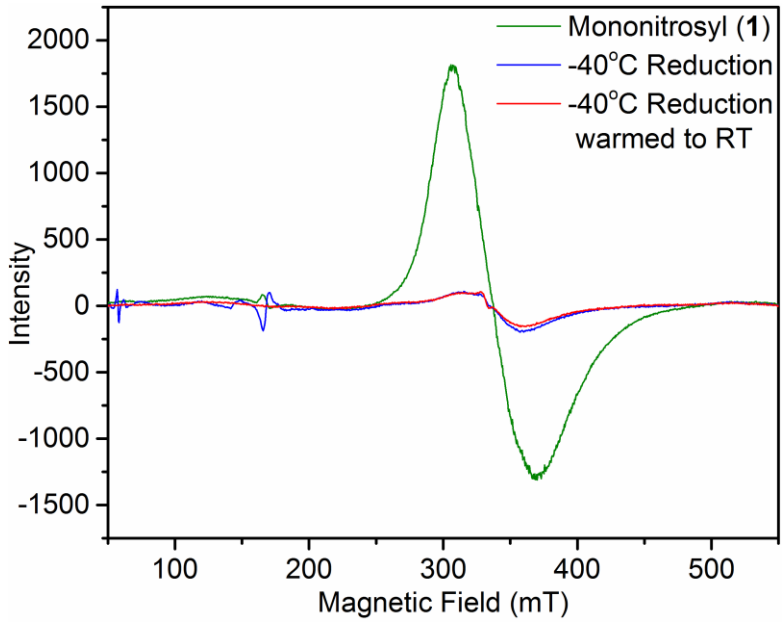

Figure 7. EPR study for the reaction of the mononitrosyldiiron(II) complex, **1** (<g> = 1.97), with excess Cp_2Co in MeCN. Conditions: [**1**] = ~2mM, [Cp_2Co] = ~4 mM, 9.355 GHz microwave frequency, 20.510 mW microwave power, 1 G modulation amplitude and 10.24 ms time constant.

superreduced mechanism to generate N_2O, the dinitrosyl diiron(II) complex uses a semireduced mechanism upon chemical reduction. A semireduced mechanism has recently been reported by two of us (N. L. and F. M.) for the dinitrosyl complex $[Fe_2(BPMP)(OPr)(NO)_2](OTf)_2$, and it has been proposed that this mechanism may constitute an efficient pathway to accomplish the reduction of NO to N_2O by synthetic catalysts as well as by FNORs.[53] We (N. L. and F. M.) have also demonstrated that the reaction of a 1:1 mixture of the natural abundance isotopes dinitrosyl diiron complex and the ^{15}NO-labeled dinitrosyl diiron complex with 1 equiv of Cp_2Co at −80 °C lead to the clean generation of solely $^{14,14}N_2O$ and $^{15,15}N_2O$ and no mixed-isotope product, consistent with an intramolecular N−N coupling reaction.[53]

Characterization of the Reduction Products. Based on the observations from the N_2O generation studies involving **1**, **2** and Cp_2Co, attempts were made to isolate and characterize the reaction product in each case. The EPR spectrum of **1** (<g> = 1.97) was essentially quenched upon reduction of **1** by excess

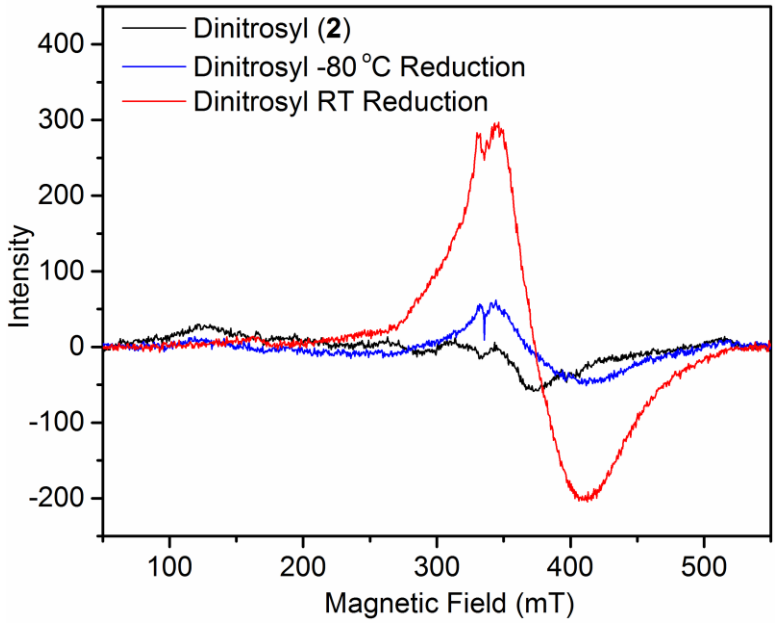

Figure 8. EPR study for the reaction of the dinitrosyl diiron(II) complex, **2** (black, 4.1 mM), with 1 eqv. Cp_2Co in CH_2Cl_2 at RT (red) and -80 ºC (blue). Conditions for reduction at RT: [**2**] = 5.1 mM, [Cp_2Co] = 5.5 mM, 9.326 GHz microwave frequency, 20.460 mW microwave power, 1 G modulation amplitude and 10.24 ms time constant. Conditions for reduction at LT (−80 °C): [**2**] = 5.4 mM, [Cp_2Co] = 5.5 mM, 9.336 GHz microwave frequency, 20.510 mW microwave power, 1 G modulation amplitude and 10.24 ms time constant.

Cp_2Co at −40°C in MeCN (Figure 7), and thus indicated the formation of a significant amount of EPR silent species during N_2O generation from **1**. The residual EPR signal with significantly low intensity may be related to the observed, low solubility of Cp_2Co in MeCN at −40°C, thereby leaving behind a small amount of unreacted **1** in the reaction mixture. Complex **2** was found to be EPR silent (Figure 8) as expected for an antiferromagnetically coupled $[\{FeNO\}^7]_2$ dimer. A mixture of **2** and 1 equiv. of Cp_2Co in CH_2Cl_2 generated a broad S = 1/2 signal (<g> = 1.55, 1.79, 2.03; see Figure S11 for the fit), with a notably higher intensity when the reaction was conducted at RT compared to LT (Figure 8) and thus indicated the formation of a mixed-valent diiron(II,III) species. Mass spectrometric analysis of a reaction mixture containing **2** and 1 eq. of Cp_2Co indeed showed the generation of a mixed-valent diiron(II, III)

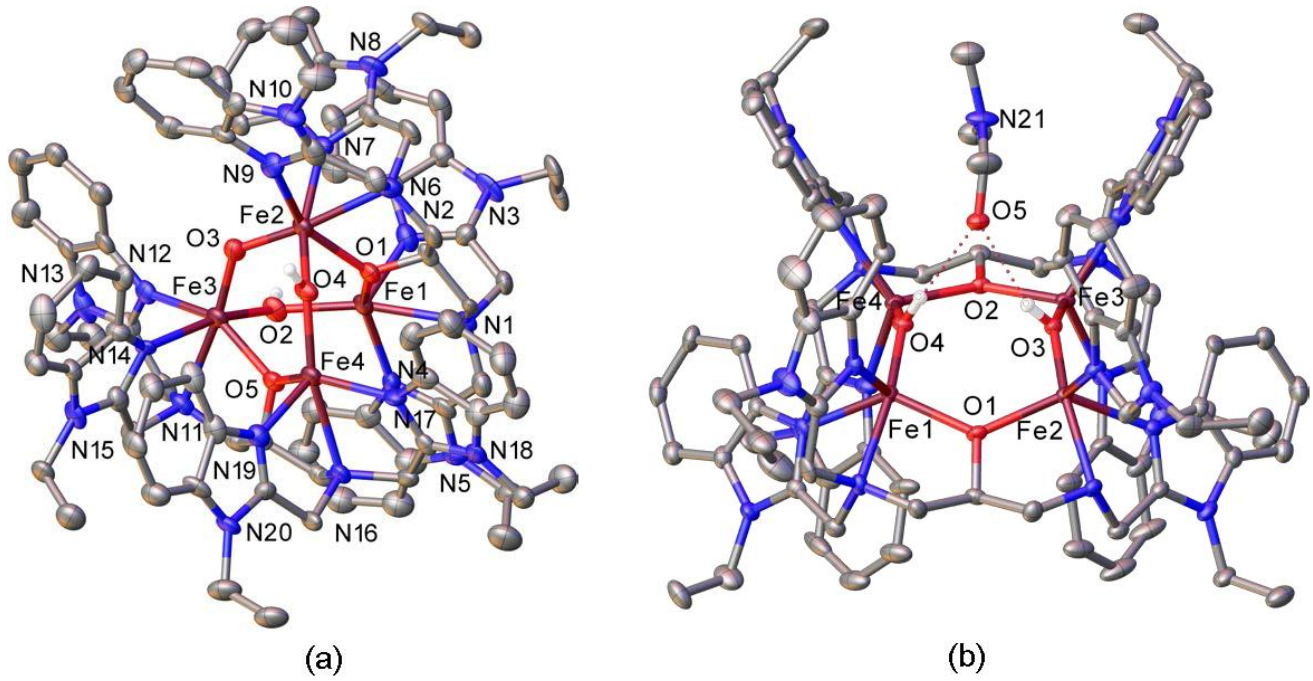

Figure 9. Molecular structures of (a) **11** and (b) **12** with 30% probability thermal ellipsoids and partial atom labeling scheme shown. Hydrogen atoms (except for the μ_2-OH groups) are omitted for clarity. Selected distances (Å): for **11**, Fe1-O2 = 2.018(9), Fe3-O2 = 1.980(8), Fe2-O4 = 1.999(9), Fe4-O4 = 1.985(8), Fe2-O3 = 1.814(8), Fe3-O3 = 1.816(8); for **12**, Fe1-O4 = 1.984(5), Fe4-O4 = 1.988(5), Fe3-O3 = 1.994(6), Fe2-O3 = 1.987(5). Selected angles (°): for **11**, <Fe1-O2-Fe3 = 120.9(4), <Fe2-O4-Fe4 = 120.6(4), <Fe2-O3-Fe3 = 130.2(5); for **12**, <Fe1-O4-Fe4 = 142.5(3), <Fe2-O3-Fe3 = 146.2(3).

complex, $[Fe_2(N\text{-Et-HPTB})(\mu\text{-O})]^{2+}$, the hydroxo-bridged dimer of the mixed-valent diiron(II,III) complex (i.e. hydroxo-bridged tetranuclear iron complexes) and Cp_2Co^+ (Figures S12 and S13), indicating that these species are direct products of the reaction, and not just formed during the crystallization experiments. Formation of such a mixed-valent diiron(II,III) species upon addition of 1 equiv. of Cp_2Co confirms a semireduction mechanism where one electron out of a total of two electrons required for the formation of N_2O (~89% yield of N_2O, Figure S9) is provided by the diiron(II) core while the second electron is provided by Cp_2Co. The mass spectrum of the bulk crystalline product obtained from the above reaction mixture also showed the presence of the mixed-valent diiron(II,III) complex, [Fe_2(*N*-Et-

HPTB)(μ-O)]$^{2+}$ and the tetranuclear iron complexes, [Fe$_4$(*N*-Et-HPTB)$_2$(μ-OH)$_3$(μ-O)]$^{3+}$ and [Fe$_4$(*N*-Et-HPTB)$_2$(μ-OH)$_2$(μ-O)]$^{4+}$ (Figure S14). The tetranuclear complexes form by dimerization of the initially formed mixed-valent diiron(II,III) complex, and these species are likely in equilibrium in solution. The bulk crystalline product contained a mixture of block-shaped crystals and (Cp$_2$Co)(BF$_4$). The block-shaped crystals were identified as [Fe$_4$(*N*-Et-HPTB)$_2$(μ-OH)$_2$(μ-O)](BF$_4$)$_4$ (**11**) by a molecular structure determination. The molecular structure of **11** (Figure 9a) features two mixed-valent diiron(II,III) units linked together by two hydroxyl bridges (average Fe–O distance = 1.995Å) and one oxo bridge (Fe–O distance = 1.815Å). On the other hand, mass spectrometric analysis of a reaction mixture containing **2** and 2 eq. of Cp$_2$Co showed the generation of Cp$_2$Co$^+$ along with a hydroxo-bridged tetranuclear iron(II) complex, [Fe$_4$(*N*-Et-HPTB)$_2$(μ-OH)$_2$]$^{4+}$, and an analogous species, [Fe$_4$(*N*-Et-HPTB)$_2$(μ-OH)$_2$(H$_2$O)]$^{4+}$ (Figure S15). The tetranuclear iron complexes form by dimerization (and protonation by H$_2$O) of the hydroxo bridged diiron(II) unit. Mass spectrometric analysis of the bulk crystalline product again showed the presence of Cp$_2$Co$^+$, [Fe$_4$(*N*-Et-HPTB)$_2$(μ-OH)$_2$]$^{4+}$ and [Fe$_4$(*N*-Et-HPTB)$_2$(μ-OH)$_2$(H$_2$O)]$^{4+}$ (Figure S16). The bulk crystalline product contained block-shaped crystals along with yellow colored needle-shaped crystals. While the needle-shaped crystals were identified as (Cp$_2$Co)(BF$_4$), molecular structure determination of the block-shaped crystals revealed a tetranuclear Fe(II) complex, [Fe$_4$(*N*-Et-HPTB)$_2$(μ-OH)$_2$](BF$_4$)$_4$ (**12**). The molecular structure of **12** (Figure 9b) shows that two diiron(II) units are bridged together via two hydroxyl groups (average Fe–O distance = 1.988Å), thus forming a tetranuclear unit. The two –OH groups are engaged in hydrogen bonding (O4H4---O5 = 2.086Å, O3H3---O5 = 2.130Å) with the oxygen atom (O5) of one DMF molecule, which is sitting on the top of the eight membered cyclic Fe1-O1-Fe2-O3-Fe3-O2-Fe4-O4 core in the crystal structure. The –OH groups and/or the proton of the –OH groups in **11** and **12** might have originated from H$_2$O, which could have been carried forward from the hydrated iron(II) salt, Fe(BF$_4$)$_2$·6H$_2$O initially used for the synthesis of **7**, which in turn was used to prepare **2**. Complexes **11** and **12**, however, could not be obtained as analytically pure samples and

therefore bulk sample characterization of these two complexes could not be accomplished. The quality of the single crystals for **11** was quite poor and led to a final R value of ~16%. Nevertheless, the isolation of **11** coupled with the EPR study (Figure 8) strongly indicates that N_2O and a mixed-valent diiron(II,III) species may be the immediate products after treatment of **2** with one equivalent of Cp_2Co, followed by dimerization of the diiron product to yield **11**. On the other hand, isolation of **12** indicates that N_2O and an oxo-bridged diiron(II) complex may be the immediate products after treatment of **2** with two equivalents of Cp_2Co. The latter may then dimerize in the presence of H_2O to finally yield **12**. Considering these results and the EPR spectroscopic study for the reaction of the mononitrosyl diiron(II) complex, **1**, with Cp_2Co (Figure 7), a similar situation is expected to be operative in the case of **1** as well. However, diffraction quality single crystals for the end products could not be isolated in the case of **1**.

In the case of complex **5**,[59] it has been observed that semireduction leads to the generation of an EPR-active, mixed-valent (S = 1/2) product when the reaction is conducted at −80 ^{o}C. However, when the reaction mixture is warmed up to RT, or the reaction is directly conducted at RT, the product becomes EPR silent, an observation that is surprising and that could not be fully explained in the initial report.[53] Our results presented above provide an elegant explanation for this finding, where the initially formed, mixed-valent (and EPR-active) Fe(II)-O-Fe(III) product would dimerize at higher temperature, producing a similar, tetrameric product as observed here (complex **11**), which is then EPR silent. This result could therefore have general implications for the behavior of mixed-valent (and diferrous) reaction products formed from NO reduction in diiron model complexes. Despite several reports on NO reduction by diiron complexes in the literature, this is the first time that the oligomerized (tetrameric) products from these reactions could be characterized unambiguously.

Proposed Mechanism. Since reduction of NO to N_2O is a two-electron reaction, complexes **1** and **2** are supposed to need 1 and 2 equivalents of reducing agents (here Cp_2Co), respectively, for the near quantitative generation of N_2O. Previously, we have proposed[55] that the generation of N_2O by **1** may

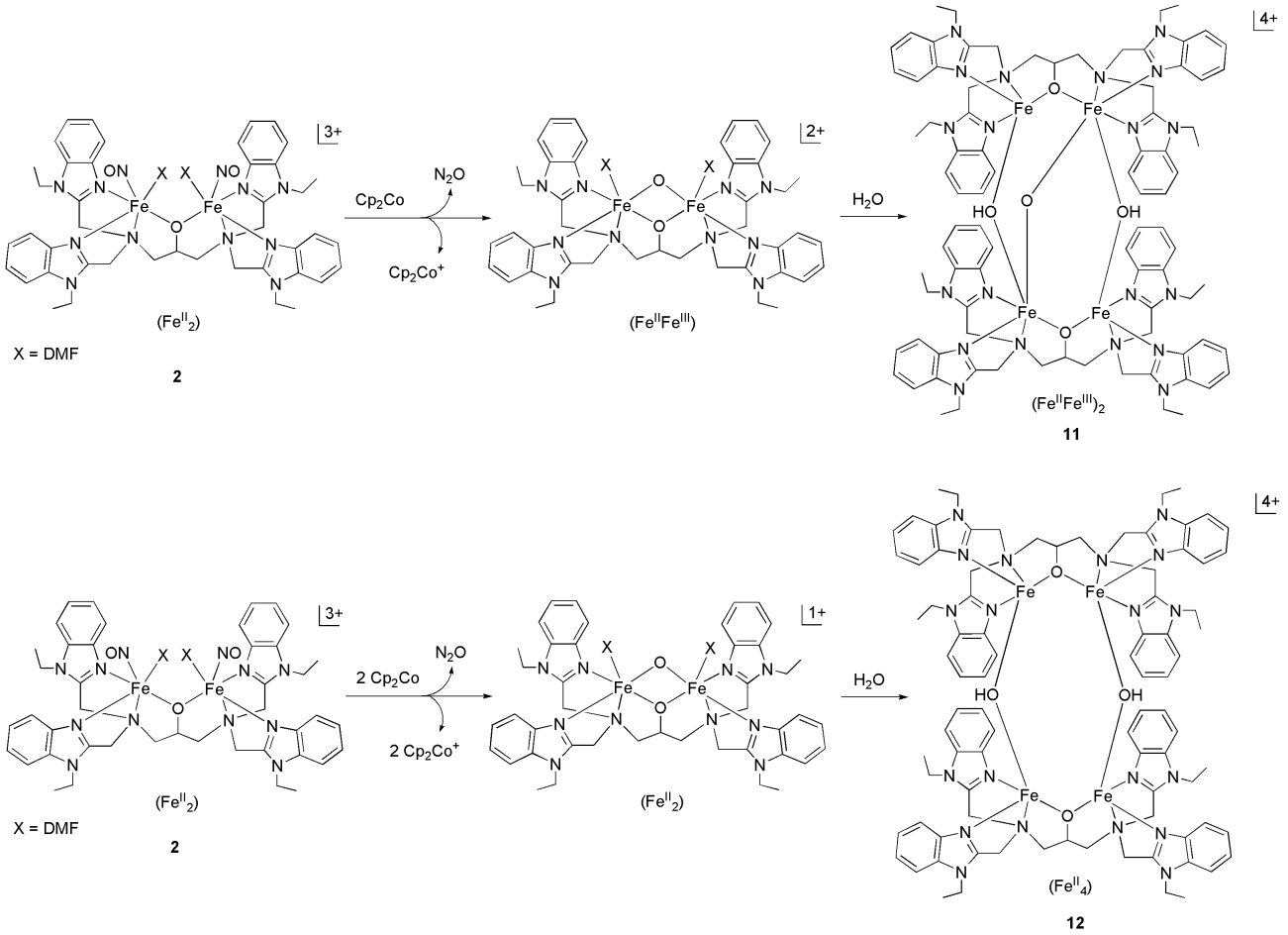

Scheme 2. Schematic presentation of the mechanism for the generation of N_2O upon reduction of **2** by 1 and 2 equivalents of cobaltocene. Complexes **2**, **11** and **12** have been characterized by single crystal x-ray structure determinations.

involve an intermolecular reaction between two molecules of the initially reduced product, [Fe^{II}{FeNO}^{8}], similar to mechanistic proposals for a mononuclear cobalt-nitrosyl complex[110] and a mononuclear, high spin {FeNO}^{8} complex.[54] An alternative pathway may, however, involve disproportionation of two molecules of [Fe^{II}{FeNO}^{8}] to one unit of **7** and [{FeNO}^{8}]$_2$, of which the latter may yield N_2O. Interestingly, it has been observed in the present work that the mononitrosyl diiron(II) complex, **1**, cannot generate N_2O in quantitative yield upon addition of only 0.5 equivalent of Cp_2Co, which only produces ~50% N_2O. In contrast, treatment of the diiron(II) dinitrosyl complex, **2**, with only 1 equivalent of Cp_2Co yields N_2O in near quantitative yield. These results strongly suggest that **2** (in contrast to **1**) is capable of

providing 1 out of the total of 2 electrons required in the reduction of 2 molecules of NO to one molecule of N_2O, and hence, these findings support a semireduced mechanism for **2**. Near quantitative (~ 89%) generation of N_2O upon treatment of **2** with 1 equivalent of Cp_2Co will, however, require oxidation of one of the Fe(II) centers to generate an EPR active (S = ½) mixed-valent diiron(II,III) species, which has been confirmed for **2** by EPR spectroscopy (Figure 8). The mixed-valent diiron(II,III) species may, however, dimerize with time to form an oxo/hydroxo-bridged tetrairon species (**11**, Scheme 2). On the other hand, generation of N_2O upon treatment of **1** and **2** by 1 and 2 equivalents (or excess) of Cp_2Co, respectively, yields an EPR silent diiron(II) species with an oxo bridge, which has been confirmed for **1** by EPR spectroscopy (Figure 7). Such a diiron(II) species may also dimerize to yield an all ferrous tetrairon complex (**12**, Scheme 2). Considering the near quantitative yields of N_2O upon reduction of **2** by 1 equiv. of Cp_2Co along with the EPR spectroscopic study and X-ray structural analysis of the reaction products, it may thus be concluded that **2** produces N_2O via a semireduced mechanism. In contrast, the mononitrosyl complex **1** can only produce N_2O using an (intermolecular) superreduced mechanism. This is an interesting dichotomy considering that **1** and **2** contain the same coligand, and hence, the $\{FeNO\}^{7/8}$ units in these complexes have very similar structural (Table S1) and electronic properties. DFT optimized structures of $\mathbf{1}^{3+}$ and $\mathbf{2}^{3+}$ contain quite typical $\{FeNO\}^7$ units with Fe-N and N-O bond lengths of 1.79 Å and 1.16 Å, respectively, and Fe-N-O bond angles of 170° in $\mathbf{1}^{3+}$ and 165° and 168° in $\mathbf{2}^{3+}$. These values are in good agreement with structural paramaters reported for these complexes (see Table 2). In contrast, the frequency calculations overestimate the Fe-NO stretching frequencies, predicting values of 1863 cm^{-1} for $\mathbf{1}^{3+}$ and antisymmetric/symmetric stretches at 1846 cm^{-1} and 1873^{-1} for $\mathbf{2}^{3+}$. Such an overestimate of the N-O stretch is typically observed with hybrid functionals such as B3LYP that contain exact Hartree-Fock exchange (see ref. 59 for more examples). Nonetheless, across the series of $\mathbf{1}^{3+/2+}$ and $\mathbf{2}^{3+/2+}$, these calculations can be employed to evaluate the differences in electronic structure between these complexes. In the calculations, reduction of $\mathbf{2}^{3+}$ to $\mathbf{2}^{2+}$ results in a significant decrease in the N-O stretching frequency

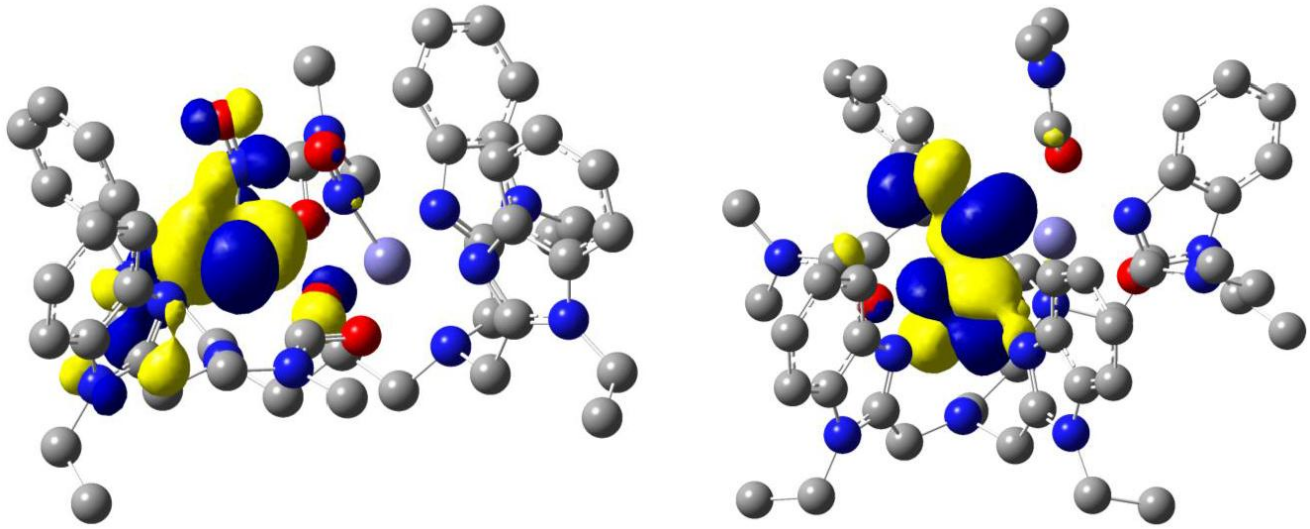

Figure 10. (Left) Contour plot of the non-bonding d_{xy} orbital (with respect to NO) that is occupied upon one-electron reduction of $\mathbf{2}^{3+}$ to $\mathbf{2}^{2+}$. Note that since the coordination environment of the two $\{FeNO\}^7$ units in $\mathbf{2}^{3+}$ is identical, with the amine groups trans to NO in both cases, reduction of the other iron center gives the same result. (Right) Contour plot of the antibonding d_{xz} orbital (with respect to NO) that is occupied upon reduction of $\mathbf{1}^{3+}$ to $\mathbf{1}^{2+}$.

of the resulting $\{FeNO\}^8$ unit to 1694 cm^{-1}. Single point calculations on the optimized structure suggest that the added electron populates the d_{xy} orbital, which is non-bonding with respect to the Fe-N-O unit (Figure 10, left). The additional electron density at the iron center leads to an increase of the effective nuclear charge of the Fe and in this way, weakens the Fe-NO bond (see ref. s 51, 52), resulting in the observed decrease in the N-O stretching frequency. In the case of **2**, it is therefore the proximity of the two Fe-NO units that facilitates *intra*molecular N-N bond formation and N_2O generation via attack of the reduced $\{FeNO\}^8$ unit on the proximal $\{FeNO\}^7$ unit (following a semireduced mechanism).[60] If the two Fe-NO units are not held in proximity, as in the mononitrosyl **1**, further activation is required. Here, attack of one $\{FeNO\}^8$ species at the $\{FeNO\}^7$ unit in a second complex is not enough to induce N-N bond formation and N_2O release. Only reaction of two $\{FeNO\}^8$ units is able to let the reaction proceed (following an *inter*molecular superreduced mechanism). This finding has mechanistic implications for

FNORs and argues against a mononitrosyl mechanism, where attack of NO on the activated $\{FeNO\}^{7/8}$ species was proposed to induce N-N bond formation. Our results indicate that this mechanistic scenario is unlikely, and that the reaction most favorably proceeds via coordination of the two NO molecules, thereby holding them in close proximity for further reaction.

In contrast to $\mathbf{2}^{2+}$, single point calculations on the optimized structure of $\mathbf{1}^{2+}$ suggest that upon reduction of the mononitrosyl complex, the extra electron occupies the antibonding $d_{xz}\_\pi^*_x$ orbital of the Fe-N-O unit (Figure 10, right). Accordingly, this induces elongation of the Fe-NO and N-O bonds to 1.90 and 1.23 Å, respectively as well as a significant increase in Fe-N-O bending, with the Fe-N-O angle decreasing from 170° to 130° (See Table S1). This is further reflected in an increase in spin density on the NO unit in $\mathbf{1}^{2+}$ compared to $\mathbf{1}^{3+}$ (See Table S2), consistent with the decreased covalency in the Fe-NO bond. Due to the decrease in Fe-NO covalency, the N-O stretching frequency in $\mathbf{1}^{2+}$ is significantly lower than that of $\mathbf{2}^{2+}$, at 1545 cm^{-1}, indicative of a more activated $\{FeNO\}^{8}$ moiety in the mononitrosyl complex. In addition, the formation of **11** and **12** after N_2O generation from **2**, may possibly indicate that such tetrameric iron complexes may in general be the end products of N_2O generation from non-heme diiron(II) model complexes of FNORs. Such tetrameric iron complexes may result by using the oxo group, generated in situ by the release of N_2O from two molecules of NO, to bridge the two diiron units. The current work thus not only reveals the different mechanisms for N_2O production from **1** and **2**, but it also explains the previously reported EPR-silent nature of the end products[53] obtained after N_2O generation. We therefore provide general insight into the fate of functional model complexes of FNORs after the reduction of NO and release of N_2O.

CONCLUSION

In summary, this work provides a detailed description of the synthesis, characterization and reactivity of a mononitrosyl diiron(II) and a dinitrosyl diiron(II) complex which may be considered as functional models for the mono- and dinitrosyl intermediates observed in the catalytic cycle of FNORs. The synthetic

rationale behind the unique and selective nitrosylation process leading to the stepwise formation of a mononitrosyl complex and its dinitrosyl analogue is explained in detail along with the inter-relationship of these complexes with a related mixed-valent diiron(II,III) and a mixed-valent mononitrosyl diiron(II,III) complex. Both the mono- and dinitrosyl diiron(II) complexes demonstrate facile N_2O generation upon chemical and electrochemical reduction following a superreduced and semireduced mechanism, respectively. This difference in reactivity points to the importance of binding two molecules of NO in close proximity for fast and efficient N_2O generation. The end products generated after N_2O release from such model complexes have been characterized by EPR spectroscopic methods and, for the first time, by single crystal X-ray structure determination, which shows the surprising formation of tetranuclear iron complexes that use the oxo/hydroxo groups produced by N_2O release as bridging ligands. This work provides, for the first time, a possible general trend for the fate of the functional model complexes of FNORs after the generation of N_2O. Furthermore, our results support the proposed semireduced mechanism as a feasible pathway for the catalytic cycle of FNORs.

ASSOCIATED CONTENT

Supporting Information.

The Supporting Information is available free of charge via the Internet at http://pubs.acs.org.

Gas chromatographic and mass spectrometric data, UV-Vis and IR Spectroscopic data, N_2O yield calculation data (PDF).

X-ray crystallographic data for **2**, **3**, **11** and **12** with CCDC numbers 1892324, 1770560, 1892326 and 1892325 respectively (cif)

AUTHOR INFORMATION

Corresponding Author

* Email: lehnertn@umich.edu; icam@iacs.res.in

ORCID

Franc Meyer: 0000-0002-8613-7862
Nicolai Lehnert: 0000-0002-5221-5498
Amit Majumdar: 0000-0003-0522-8533

Author Contributions

The manuscript was written through contributions of all authors. All authors have given approval to the final version of the manuscript. ‡These authors contributed equally.

ACKNOWLEDGMENT

This work was supported by the grant EMR/2017/000828 (SERB, India). M.J. and N.P. acknowledge CSIR, India for SRF. N.L. acknowledges funding from the National Science Foundation (NSF, CHE-1608331). C.C. and F.M. acknowledge support from the University of Göttingen (Göttingen International) and the Fonds der Chemischen Industrie (PhD scholarship for C.C.).

References.

1. Ignarro, L., *Nitric Oxide: Biology and Pathobiology*. Academic Press: San Diego, 2000.
2. Moncada, S.; Palmer, R. M.; Higgs, E. A., Nitric oxide: physiology, pathophysiology, and pharmacology. *Pharmaco. Rev.* **1991**, *43*, 109-142.
3. Missall, T. A.; Lodge, J. K.; McEwen, J. E., Mechanisms of Resistance to Oxidative and Nitrosative Stress: Implications for Fungal Survival in Mammalian Hosts. *Eukaryot. Cell* **2004**, *3*, 835-846.
4. Arkenberg, A.; Runkel, S.; Richardson, D. J.; Rowley, G., The production and detoxification of a potent cytotoxin, nitric oxide, by pathogenic enteric bacteria. *Biochem. Soc. Trans.* **2011**, *39*, 1876-1879.
5. Nathan, C., Inducible nitric oxide synthase: What difference does it make? *J. Clin. Invest.* **1997**, *100*, 2417-2423.
6. MacMicking, J.; Xie, Q. W.; Nathan, C., Nitric oxide and macrophage function. *Annu. Rev. Immunol.* **1997**, *15*, 323-350.
7. Hayashi, T.; Caranto, J. D.; Wampler, D. A.; Kurtz, D. M., Jr.; Moënne-Loccoz, P., Insights into the Nitric Oxide Reductase Mechanism of Flavodiiron Proteins from a Flavin-Free Enzyme. *Biochemistry* **2010**, *49*, 7040-7049.
8. Silaghi-Dumitrescu, R.; Kurtz, D. M., Jr.; Ljungdahl, L. G.; Lanzilotta, W. N., X-ray Crystal Structures of Moorella thermoacetica FprA. Novel Diiron Site Structure and Mechanistic Insights into a Scavenging Nitric Oxide Reductase. *Biochemistry* **2005**, *44*, 6492-6501.
9. Frazao, C.; Silva, G.; Gomes, C. M.; Matias, P.; Coelho, R.; Sieker, L.; Macedo, S.; Liu, M. Y.; Oliveira, S.; Teixeira, M.; Xavier, A. V.; Rodrigues-Pousada, C.; Carrondo, M. A.; Le Gall, J., Structure of a dioxygen reduction enzyme from Desulfovibrio gigas. *Nat. Struct. Mol. Biol.* **2000**, *7*, 1041-1045.
10. Khatua, S.; Majumdar, A., Flavodiiron nitric oxide reductases: Recent developments in the mechanistic study and model chemistry for the catalytic reduction of NO. *J. Inorg. Biochem.* **2015**, *142*, 145-153.
11. Kurtz, D. M., Jr., Flavo-diiron enzymes: nitric oxide or dioxygen reductases? *Dalton Trans.* **2007**, 4115-4121.
12. Berto, T. C.; Speelman, A. L.; Zheng, S.; Lehnert, N., Mono- and dinuclear non-heme iron–nitrosyl complexes: Models for key intermediates in bacterial nitric oxide reductases. *Coord. Chem. Rev.* **2013**, *257*, 244-259.
13. Lehnert, N.; Fujisawa, K.; Camarena, S.; Dong, H. T.; White, C. J., Activation of Non-Heme Iron-Nitrosyl Complexes: Turning Up the Heat. *ACS Catal.* **2019**, *9*, 10499-10518.
14. Gardner, A. M.; Helmick, R. A.; Gardner, P. R., Flavorubredoxin, an Inducible Catalyst for Nitric Oxide Reduction and Detoxification in Escherichia coli. *J. Biol. Chem.* **2002**, *277*, 8172-8177.
15. Kurtz, D. M., Jr., Structural similarity and functional diversity in diiron-oxo proteins. *J. Biol. Inorg. Chem.* **1997**, *2*, 159-167.
16. Sarti, P.; Fiori, P. L.; Forte, E.; Rappelli, P.; Teixeira, M.; Mastronicola, D.; Sanciu, G.; Giuffré, A.; Brunori, M., Trichomonas vaginalis degrades nitric oxide and expresses a flavorubredoxin-like protein: a new pathogenic mechanism? *Cell. Mol. Life Sci.* **2004**, *61*, 618-623.
17. Vine, C. E.; Cole, J. A., Unresolved sources, sinks, and pathways for the recovery of enteric bacteria from nitrosative stress. *FEMS Microbiol. Lett.* **2011**, *325*, 99-107.
18. Rodrigues, R.; Vicente, J. B.; Félix, R.; Oliveira, S.; Teixeira, M.; Rodrigues-Pousada, C., Desulfovibrio gigas Flavodiiron Protein Affords Protection against Nitrosative Stress In Vivo. *J. Bacteriol.* **2006**, *188*, 2745-2751.
19. Mills, P. C.; Rowley, G.; Spiro, S.; Hinton, J. C. D.; Richardson, D. J., A combination of cytochrome c nitrite reductase (NrfA) and flavorubredoxin (NorV) protects Salmonella enterica serovar Typhimurium against killing by NO in anoxic environments. *Microbiology* **2008**, *154*, 1218-1228.

20. Kern, M.; Volz, J.; Simon, J., The oxidative and nitrosative stress defence network of Wolinella succinogenes: cytochrome c nitrite reductase mediates the stress response to nitrite, nitric oxide, hydroxylamine and hydrogen peroxide. *Environ. Microbiol.* **2011**, *13*, 2478-2494.
21. Wasserfallen, A.; Ragettli, S.; Jouanneau, Y.; Leisinger, T., A family of flavoproteins in the domains Archaea and Bacteria. *Eur. J. Biochem.* **1998**, *254*, 325-332.
22. Saraiva, L. M.; Vicente, J. B.; Teixeira, M., The Role of the Flavodiiron Proteins in Microbial Nitric Oxide Detoxification. In *Advances in Microbial Physiology*, Academic Press: 2004; Vol. Volume 49, 77-129.
23. Thorgersen, M. P.; Stirrett, K.; Scott, R. A.; Adams, M. W. W., Mechanism of oxygen detoxification by the surprisingly oxygen-tolerant hyperthermophilic archaeon, Pyrococcus furiosus. *Proc. Natl. Acad. Sci.* **2012**, *109*, 18547-18552.
24. Vicente, J. B.; Tran, V.; Pinto, L.; Teixeira, M.; Singh, U., A Detoxifying Oxygen Reductase in the Anaerobic Protozoan Entamoeba histolytica. *Eukaryot. Cell* **2012**, *11*, 1112-1118.
25. Le Fourn, C.; Brasseur, G.; Brochier-Armanet, C.; Pieulle, L.; Brioukhanov, A.; Ollivier, B.; Dolla, A., An oxygen reduction chain in the hyperthermophilic anaerobe Thermotoga maritima highlights horizontal gene transfer between Thermococcales and Thermotogales. *Environ. Microbiol.* **2011**, *13*, 2132-2145.
26. Hillmann, F.; Riebe, O.; Fischer, R. J.; Mot, A.; Caranto, J. D.; Kurtz, D. M.; Bahl, H., Reductive dioxygen scavenging by flavo-diiron proteins of Clostridium acetobutylicum. *FEBS Lett.* **2009**, *583*, 241-245.
27. Gardner, A. M.; Gardner, P. R., Flavohemoglobin Detoxifies Nitric Oxide in Aerobic, but Not Anaerobic, Escherichia coli : Evidence for A Novel Inducible Anaerobic Nitric Oxide Scavenging Activity. *J. Biol. Chem.* **2002**, *277*, 8166-8171.
28. Silaghi-Dumitrescu, R.; Ng, K. Y.; Viswanathan, R.; Kurtz, D. M., A Flavo-Diiron Protein from Desulfovibrio vulgaris with Oxidase and Nitric Oxide Reductase Activities. Evidence for an in Vivo Nitric Oxide Scavenging Function. *Biochemistry* **2005**, *44*, 3572-3579.
29. Das, A.; Coulter, E. D.; Kurtz Jr., D. M.; Ljungdahl, L. G., Five-Gene Cluster in Clostridium thermoaceticumConsisting of Two Divergent Operons Encoding Rubredoxin Oxidoreductase-Rubredoxin and Rubrerythrin–Type A Flavoprotein– High-Molecular-Weight Rubredoxin. *J. Bacteriol.* **2001**, *183*, 1560-1567.
30. Silaghi-Dumitrescu, R.; Coulter, E. D.; Das, A.; Ljungdahl, L. G.; Jameson, G. N. L.; Huynh, B. H.; Kurtz, D. M., A Flavodiiron Protein and High Molecular Weight Rubredoxin from Moorella thermoacetica with Nitric Oxide Reductase Activity. *Biochemistry* **2003**, *42*, 2806-2815.
31. Fang, H.; Caranto, J.; Mendoza, R.; Taylor, A.; Hart, P. J.; Kurtz, D., Jr., Histidine ligand variants of a flavo-diiron protein: effects on structure and activities. *J. Biol. Inorg. Chem.* **2012**, *17*, 1231-1239.
32. Blomberg, L. M.; Blomberg, M. A.; Siegbahn, P. M., Theoretical study of the reduction of nitric oxide in an A-type flavoprotein. *J. Biol. Inorg. Chem.* **2007**, *12*, 79-89.
33. Caranto, J. D.; Weitz, A.; Hendrich, M. P.; Kurtz, D. M., The Nitric Oxide Reductase Mechanism of a Flavo-Diiron Protein: Identification of Active-Site Intermediates and Products. *J. Am. Chem. Soc.* **2014**, *136*, 7981-7992.
34. APEX II 2009 Ed.; Bruker Analytical X-ray Systems Inc.: Madison, WI, 2009.
35. Speelman, A. L.; Lehnert, N., Heme versus Non-Heme Iron-Nitroxyl $\{FeN(H)O\}^8$ Complexes: Electronic Structure and Biologically Relevant Reactivity. *Acc. Chem. Res.* **2014**, *47*, 1106-1116.
36. Hayashi, T.; Caranto, J. D.; Matsumura, H.; Kurtz, D. M., Jr.; Moënne-Loccoz, P., Vibrational Analysis of Mononitrosyl Complexes in Hemerythrin and Flavodiiron Proteins: Relevance to Detoxifying NO Reductase. *J. Am. Chem. Soc.* **2012**, *134*, 6878-6884.

37. Enemark, J. H.; Feltham, R. D., Principles of structure, bonding, and reactivity for metal nitrosyl complexes. *Coord. Chem. Rev.* **1974**, *13*, 339-406.
38. Bill, E.; Bernhardt, F.-H.; Trautwein, A. X.; Winkler, H., Mössbauer investigation of the cofactor iron of putidamonooxin. *Eur. J. Biochem.* **1985**, *147*, 177-182.
39. Pohl, K.; Wieghardt, K.; Nuber, B.; Weiss, J., Preparation and magnetism of the binuclear iron(II) complexes [{Fe($C_9H_{21}N_3$)X_2}$_2$](X = NCS, NCO, or N_3) and their reaction with NO. Crystal structures of [{Fe($C_9H_{21}N_3$)(NCS)$_2$}$_2$] and [Fe($C_9H_{21}N_3$)(NO)(N_3)$_2$]. *J. Chem. Soc., Dalton Trans.* **1987**, 187-192.
40. Wells, F. V.; McCann, S. W.; Wickman, H. H.; Kessel, S. L.; Hendrickson, D. N.; Feltham, R. D., Moessbauer effect and magnetic investigation of the S = 3/2 .tautm. S = 1/2 spin crossover in [Fe(salen)NO] and the S = 3/2 state in [Fe(5-salen)NO]. *Inorg. Chem.* **1982**, *21*, 2306-2311.
41. Salerno, J. C.; Siedow, J. N., Nature of the Nitric Oxide Complexes of Lipoxygenase. *Biochim. Biophys. Acta* **1979**, *579*, 246-251.
42. Earnshaw, A.; King, E. A.; Larkwort, L., Transition Metal-Schiffs Base Complexes .V. Spin Equilibria in Some Iron Mononitrosyls. *J. Chem. Soc. A -Inorg. Phys. Theor.* **1969**, 2459-2463.
43. Slappendel, S.; Veldink, G. A.; Vliegenthart, J. F. G.; Aasa, R.; Malmstrom, B. G., A Quantitative Optical and Electron-Paramagnetic-Res Study on the Interaction Between Soyabean Lipoxygenase-1 and 13-L-Hydroperoxylinoleic Acid. *Biochim. Biophys. Acta* **1983**, *747*, 32-36.
44. Zhang, Y.; Pavlosky, M. A.; Brown, C. A.; Westre, T. E.; Hedman, B.; Hodgson, K. O.; Solomon, E. I., Spectroscopic and theoretical description of the electronic structure of the S = 3/2 nitrosyl complex of non-heme iron enzymes. *J. Am. Chem. Soc.* **1992**, *114*, 9189-9191.
45. Brown, C. A.; Pavlosky, M. A.; Westre, T. E.; Zhang, Y.; Hedman, B.; Hodgson, K. O.; Solomon, E. I., Spectroscopic and Theoretical Description of the Electronic Structure of S = 3/2 Iron-Nitrosyl Complexes and Their Relation to O_2 Activation by Non-Heme Iron Enzyme Active Sites. *J. Am. Chem. Soc.* **1995**, *117*, 715-732.
46. Diebold, A. R.; Brown-Marshall, C. D.; Neidig, M. L.; Brownlee, J. M.; Moran, G. R.; Solomon, E. I., Activation of α-Keto Acid-Dependent Dioxygenases: Application of an $\{FeNO\}^7/\{FeO_2\}^8$ Methodology for Characterizing the Initial Steps of O_2 Activation. *J. Am. Chem. Soc.* **2011**, *133*, 18148-18160.
47. Ray, M.; Golombek, A. P.; Hendrich, M. P.; Yap, G. P. A.; Liable-Sands, L. M.; Rheingold, A. L.; Borovik, A. S., Structure and Magnetic Properties of Trigonal Bipyramidal Iron Nitrosyl Complexes. *Inorg. Chem.* **1999**, *38*, 3110-3115.
48. Serres, R. G.; Grapperhaus, C. A.; Bothe, E.; Bill, E.; Weyhermüller, T.; Neese, F.; Wieghardt, K., Structural, Spectroscopic, and Computational Study of an Octahedral, Non-Heme $\{Fe{-}NO\}^{6-8}$ Series: $[Fe(NO)(cyclam\text{-}ac)]^{2+/+/0}$. *J. Am. Chem. Soc.* **2004**, *126*, 5138-5153.
49. Jackson, T. A.; Yikilmaz, E.; Miller, A.-F.; Brunold, T. C., Spectroscopic and Computational Study of a Non-Heme Iron $\{Fe{-}NO\}^7$ System: Exploring the Geometric and Electronic Structures of the Nitrosyl Adduct of Iron Superoxide Dismutase. *J. Am. Chem. Soc.* **2003**, *125*, 8348-8363.
50. Ye, S.; Price, J. C.; Barr, E. W.; Green, M. T.; Bollinger, J. M.; Krebs, C.; Neese, F., Cryoreduction of the NO-Adduct of Taurine:α-Ketoglutarate Dioxygenase (TauD) Yields an Elusive $\{FeNO\}^8$ Species. *J. Am. Chem. Soc.* **2010**, *132*, 4739-4751.
51. Berto, T. C.; Hoffman, M. B.; Murata, Y.; Landenberger, K. B.; Alp, E. E.; Zhao, J.; Lehnert, N., Structural and Electronic Characterization of Non-Heme Fe(II)–Nitrosyls as Biomimetic Models of the FeB Center of Bacterial Nitric Oxide Reductase. *J. Am. Chem. Soc.* **2011**, *133*, 16714-16717.
52. Speelman, A. L.; Lehnert, N., Characterization of a High-Spin Non-Heme $\{FeNO\}^8$ Complex: Implications for the Reactivity of Iron Nitroxyl Species in Biology. *Angew. Chem. Int. Ed.* **2013**, *52*, 12283-12287.

53. White, C. J.; Speelman, A. L.; Kupper, C.; Demeshko, S.; Meyer, F.; Shanahan, J. P.; Alp, E. E.; Hu, M.; Zhao, J.; Lehnert, N., The Semireduced Mechanism for Nitric Oxide Reduction by Non-Heme Diiron Complexes: Modeling Flavodiiron Nitric Oxide Reductases. *J. Am. Chem. Soc.* **2018**, *140*, 2562-2574.
54. Confer, A. M.; McQuilken, A. C.; Matsumura, H.; Moënne-Loccoz, P.; Goldberg, D. P., A Nonheme, High-Spin $\{FeNO\}^8$ Complex that Spontaneously Generates N_2O. *J. Am. Chem. Soc.* **2017**, *139*, 10621-10624.
55. Jana, M.; Pal, N.; White, C. J.; Kupper, C.; Meyer, F.; Lehnert, N.; Majumdar, A., Functional Mononitrosyl Diiron(II) Complex Mediates the Reduction of NO to N_2O with Relevance for Flavodiiron NO Reductases. *J. Am. Chem. Soc.* **2017**, *139*, 14380-14383.
56. Caranto, J. D.; Weitz, A.; Giri, N.; Hendrich, M. P.; Kurtz, D. M., A Diferrous-Dinitrosyl Intermediate in the N_2O-Generating Pathway of a Deflavinated Flavo-Diiron Protein. *Biochemistry* **2014**, *53*, 5631-5637.
57. Dong, H. T.; White, C. J.; Zhang, B.; Krebs, C.; Lehnert, N., Non-Heme Diiron Model Complexes Can Mediate Direct NO Reduction: Mechanistic Insight into Flavodiiron NO Reductases. *J. Am. Chem. Soc.* **2018**, *140*, 13429-13440.
58. Feig, A. L.; Bautista, M. T.; Lippard, S. J., A Carboxylate-Bridged Non-Heme Diiron Dinitrosyl Complex. *Inorg. Chem.* **1996**, *35*, 6892-6898.
59. Zheng, S.; Berto, T. C.; Dahl, E. W.; Hoffman, M. B.; Speelman, A. L.; Lehnert, N., The Functional Model Complex $[Fe_2(BPMP)(OPr)(NO)_2](BPh_4)_2$ Provides Insight into the Mechanism of Flavodiiron NO Reductases. *J. Am. Chem. Soc.* **2013**, *135*, 4902-4905.
60. Van Stappen, C.; Lehnert, N., Mechanism of N–N Bond Formation by Transition Metal–Nitrosyl Complexes: Modeling Flavodiiron Nitric Oxide Reductases. *Inorg. Chem.* **2018**, *57*, 4252-4269.
61. Wright, A. M.; Hayton, T. W., Understanding the Role of Hyponitrite in Nitric Oxide Reduction. *Inorg. Chem.* **2015**, *54*, 9330-9341.
62. Arikawa, Y.; Onishi, M., Reductive N–N coupling of NO molecules on transition metal complexes leading to N_2O. *Coord. Chem. Rev.* **2012**, *256*, 468-478.
63. Wright, A. M.; Wu, G.; Hayton, T. W., Formation of N_2O from a Nickel Nitrosyl: Isolation of the cis-$[N_2O_2]^{2-}$ Intermediate. *J. Am. Chem. Soc.* **2012**, *134*, 9930-9933.
64. Wright, A. M.; Zaman, H. T.; Wu, G.; Hayton, T. W., Mechanistic Insights into the Formation of N_2O by a Nickel Nitrosyl Complex. *Inorg. Chem.* **2014**, *53*, 3108-3116.
65. Jeżowska-Trzebiatowska, B.; Hanuza, J.; Ostern, M.; Ziółkowski, J., The nature of bonding and the structure of pentacyanonitrosylcobaltate(III) on the basis of infra-red and electronic spectroscopy. *Inorg. Chim. Acta* **1972**, *6*, 141-144.
66. Arikawa, Y.; Asayama, T.; Moriguchi, Y.; Agari, S.; Onishi, M., Reversible N−N Coupling of NO Ligands on Dinuclear Ruthenium Complexes and Subsequent N_2O Evolution: Relevance to Nitric Oxide Reductase. *J. Am. Chem. Soc.* **2007**, *129*, 14160-14161.
67. Arikawa, Y.; Matsumoto, N.; Asayama, T.; Umakoshi, K.; Onishi, M., Conversion of oxido-bridged dinuclear ruthenium complex to dicationic dinitrosyl ruthenium complex using proton and nitric oxide: Completion of NO reduction cycle. *Dalton Trans.* **2011**, *40*, 2148-2150.
68. Ferretti, E.; Dechert, S.; Demeshko, S.; Holthausen, M. C.; Meyer, F., Reductive Nitric Oxide Coupling at a Dinickel Core: Isolation of a Key cis-Hyponitrite Intermediate en route to N_2O Formation. *Angew. Chem. Int. Ed.* **2019**, *58*, 1705-1709.
69. Kundu, S.; Phu, P. N.; Ghosh, P.; Kozimor, S. A.; Bertke, J. A.; Stieber, S. C. E.; Warren, T. H., Nitrosyl Linkage Isomers: NO Coupling to N_2O at a Mononuclear Site. *J. Am. Chem. Soc.* **2019**, *141*, 1415-1419.

70. Wasser, I. M.; de Vries, S.; Moënne-Loccoz, P.; Schröder, I.; Karlin, K. D., Nitric Oxide in Biological Denitrification: Fe/Cu Metalloenzyme and Metal Complex NOx Redox Chemistry. *Chem. Rev.* **2002**, *102*, 1201-1234.
71. Jiang, Y.; Hayashi, T.; Matsumura, H.; Do, L. H.; Majumdar, A.; Lippard, S. J.; Moënne-Loccoz, P., Light-induced N_2O production from a nonheme iron-nitrosyl dimer. *J. Am. Chem. Soc.* **2014**, *136*, 12524-12527.
72. Kindermann, N.; Schober, A.; Demeshko, S.; Lehnert, N.; Meyer, F., Reductive Transformations of a Pyrazolate-Based Bioinspired Diiron–Dinitrosyl Complex. *Inorg. Chem.* **2016**, *55*, 11538-11550.
73. Majumdar, A.; Apfel, U.-P.; Jiang, Y.; Moënne-Loccoz, P.; Lippard, S. J., Versatile Reactivity of a Solvent-Coordinated Diiron(II) Compound: Synthesis and Dioxygen Reactivity of a Mixed-Valent $Fe^{II}Fe^{III}$ Species. *Inorg. Chem.* **2014**, *53*, 167-181.
74. Pal, N.; Majumdar, A., Controlling the Reactivity of Bifunctional Ligands: Carboxylate-Bridged Nonheme Diiron(II) Complexes Bearing Free Thiol Groups. *Inorg. Chem.* **2016**, *55*, 3181-3191.
75. Majumdar, A.; Lippard, S. J., Non-Heme Mononitrosyldiiron Complexes: Importance of Iron Oxidation State in Controlling the Nature of the Nitrosylated Products. *Inorg. Chem.* **2013**, *52*, 13292-13294.
76. McKee, V.; Zvagulis, M.; Dagdigian, J. V.; Patch, M. G.; Reed, C. A., Hemocyanin Models-Synthesis, Structure, and Magnetic Properties of a Binucleating Copper(II) System. *J. Am. Chem. Soc.* **1984**, *106*, 4765-4772.
77. Borovik, A. S.; Papaefthymiou, V.; Taylor, L. F.; Anderson, O. P.; Que, L., Models for iron-oxo proteins. Structures and properties of $Fe^{II}Fe^{III}$, $Zn^{II}Fe^{III}$, and $Fe^{II}Ga^{III}$ complexes with (μ-phenoxo)bis(μ-carboxylato)dimetal cores. *J. Am. Chem. Soc.* **1989**, *111*, 6183-6195.
78. Suzuki, M.; Kanatomi, H.; Murase, I., Synthesis and Properties of Binuclear Cobalt(II) Oxygen Adduct with 2,6-Bis[Bis(2-pyridylmethyl)Aminomethyl]-4-Methylphenol. *Chem. Lett.* **1981**, *10*, 1745-1748.
79. Armarego, W. L. F.; Chai, C. L. L., *Purification of Laboratory Chemicals*. Sixth ed.; Butterworth-Heinemann, Elsevier Inc.: USA, 2009.
80. Harrop, T. C.; Tonzetich, Z. J.; Reisner, E.; Lippard, S. J., Reactions of Synthetic [2Fe-2S] and [4Fe-4S] Clusters with Nitric Oxide and Nitrosothiols. *J. Am. Chem. Soc.* **2008**, *130*, 15602-15610.
81. Arulsamy, N.; Bohle, D. S.; Butt, J. A.; Irvine, G. J.; Jordan, P. A.; Sagan, E., Interrelationships between Conformational Dynamics and the Redox Chemistry of S-Nitrosothiols. *J. Am. Chem. Soc.* **1999**, *121*, 7115-7123.
82. M. J. Frisch, G. W. T., H. B. Schlegel, G. E. Scuseria, ; M. A. Robb, J. R. C., G. Scalmani, V. Barone, B. Mennucci, ; G. A. Petersson, H. N., M. Caricato, X. Li, H. P. Hratchian, ; A. F. Izmaylov, J. B., G. Zheng, J. L. Sonnenberg, M. Hada, ; M. Ehara, K. T., R. Fukuda, J. Hasegawa, M. Ishida, T. Nakajima, ; Y. Honda, O. K., H. Nakai, T. Vreven, J. A. Montgomery, Jr., ; J. E. Peralta, F. O., M. Bearpark, J. J. Heyd, E. Brothers, ; K. N. Kudin, V. N. S., T. Keith, R. Kobayashi, J. Normand, ; K. Raghavachari, A. R., J. C. Burant, S. S. Iyengar, J. Tomasi, ; M. Cossi, N. R., J. M. Millam, M. Klene, J. E. Knox, J. B. Cross, ; V. Bakken, C. A., J. Jaramillo, R. Gomperts, R. E. Stratmann, ; O. Yazyev, A. J. A., R. Cammi, C. Pomelli, J. W. Ochterski, ; R. L. Martin, K. M., V. G. Zakrzewski, G. A. Voth, ; P. Salvador, J. J. D., S. Dapprich, A. D. Daniels, ; O. Farkas, J. B. F., J. V. Ortiz, J. Cioslowski, ; Fox, D. J. *Gaussian 09, Revision E.01*, Wallingford, CT, 2013.
83. Becke, A. D., Density-functional thermochemistry. III. The role of exact exchange. *J. Chem. Phys.* **1993**, *98*, 5648-5652.
84. Lee, C.; Yang, W.; Parr, R. G., Development of the Colle-Salvetti correlation-energy formula into a functional of the electron density. *Phys. Rev. B* **1988**, *37*, 785-789.
85. Perdew, J. P.; Burke, K.; Wang, Y., Generalized gradient approximation for the exchange-correlation hole of a many-electron system. *Physical Review B* **1996**, *54*, 16533-16539.

86. Wachters, A. J. H., Gaussian Basis Set for Molecular Wavefunctions Containing Third-Row Atoms. *J. Chem. Phys.* **1970**, *52*, 1033-1036.
87. Hay, P. J., Gaussian basis sets for molecular calculations. The representation of 3d orbitals in transition-metal atoms. *J. Chem. Phys.* **1977**, *66*, 4377-4384.
88. Bill, E. *julX, Program for Simulation of Molecular Magnetic Data*, Max-Planck Institute for Chemical Energy Conversion, Mülheim/Ruhr, 2008.
89. Neese, F., Software update: the ORCA program system, version 4.0. *Wiley Interdisciplinary Reviews: Computational Molecular Science* **2018**, *8*, e1327.
90. Weigend, F., Accurate Coulomb-fitting basis sets for H to Rn. *Phys. Chem. Chem. Phys.* **2006**, *8*, 1057-1065.
91. Spek, A. L., Single-crystal structure validation with the program PLATON. *J. Appl. Crystallogr.* **2003**, *36*, 7-13.
92. Spek, A. L., Structure validation in chemical crystallography. *Acta Crystallogr. Sect. D* **2009**, *65*, 148-155.
93. Sheldrick, G. M., A short history of SHELX. *Acta Crystallogr. Sect. A* **2008**, *64*, 112-122.
94. Dolomanov, O. V.; Bourhis, L. J.; Gildea, R. J.; Howard, J. A. K.; Puschmann, H., OLEX2: a complete structure solution, refinement and analysis program. *J. Appl. Crystallogr.* **2009**, *42*, 339-341.
95. Farrugia, L. J., ORTEP-3 for Windows-a version of ORTEP-III with a Graphical User Interface (GUI) *J. Appl. Crystallogr.* **1997**, *30*, 565.
96. Farrugia, L. J., WinGX and ORTEP for Windows: an update. *J. Appl. Crystallogr.* **2012**, *45*, 849-854.
97. Stamler, J. S.; Singel, D. J.; Loscalzo, J., Biochemistry of nitric oxide and its redox-activated forms. *Science* **1992**, *258*, 1898-1902.
98. Rhine, M. A.; Sanders, B. C.; Patra, A. K.; Harrop, T. C., Overview and New Insights into the Thiol Reactivity of Coordinated NO in $\{MNO\}^{6/7/8}$ (M = Fe, Co) Complexes. *Inorg. Chem.* **2015**, *54*, 9351-9366.
99. Zhao, R.; Lind, J.; Merényi, G.; Eriksen, T. E., One-Electron Reduction Potential and the β-Fragmentation of Acetylthiyl Radical, Comparisons with Benzoylthiyl Radical and the Oxygen Counterparts. *J. Phys. Chem. A* **1999**, *103*, 71-74.
100. Liu, R.; Orgel, L. E., Oxidative acylation using thioacids. *Nature* **1997**, *389*, 52-54.
101. Dong, Y.; Menage, S.; Brennan, B. A.; Elgren, T. E.; Jang, H. G.; Pearce, L. L.; Que, L., Jr., Dioxygen Binding to Diferrous Centers - Models For Diiron Oxo Proteins. *J. Am. Chem. Soc.* **1993**, *115*, 1851-1859.
102. Speelman, A. L.; White, C. J.; Zhang, B.; Alp, E. E.; Zhao, J.; Hu, M.; Krebs, C.; Penner-Hahn, J.; Lehnert, N., Non-heme High-Spin $\{FeNO\}^{6-8}$ Complexes: One Ligand Platform Can Do It All. *J. Am. Chem. Soc.* **2018**, *140*, 11341-11359.
103. Borovik, A. S.; Que, L., Jr., Models for the $Fe^{II}Fe^{III}$ and $Fe^{II}Fe^{II}$ Forms of Iron-Oxo Proteins. *J. Am. Chem. Soc.* **1988**, *110*, 2345-2347.
104. Suzuki, M.; Uehara, A.; Oshio, H.; Endo, K.; Yanaga, M.; Kida, S.; Saito, K., Synthesis and Characterization of Dinuclear Iron(II, II) and Iron(II, III) Complexes with a Dinucleating Ligand, 2,6-Bis Bis(2-Pyridylmethyl)-Aminomethyl -4-Mmethylphenolate (1-). *Bull. Chem. Soc. Jpn.* **1987**, *60*, 3547-3555.
105. Borovik, A. S.; Murch, B. P.; Que, L., Jr.; Papaefthymiou, V.; Munck, E., Models for Iron Oxo Proteins - A Mixed-Valence Iron(II)-Iron(III) Complex. *J. Am. Chem. Soc.* **1987**, *109*, 7190-7191.
106. Li, F.; Chakrabarti, M.; Dong, Y.; Kauffmann, K.; Bominaar, E. L.; Münck, E.; Que, L., Jr., Structural, EPR, and Mössbauer Characterization of (μ-Alkoxo)(μ-Carboxylato)Diiron(II,III) Model Complexes for the Active Sites of Mixed-Valent Diiron Enzymes. *Inorg. Chem.* **2012**, *51*, 2917-2929.

107. Hartman, J. A. R.; Rardin, R. L.; Chaudhuri, P.; Pohl, K.; Wieghardt, K.; Nuber, B.; Weiss, J.; Papaefthymiou, G. C.; Frankel, R. B.; Lippard, S. J., Synthesis and Characterization of (μ-hydroxo)bis(μ-acetato)diiron(II) and (μ-oxo)bis(μ-acetato)diiron(III) 1,4,7-trimethyl-1,4,7-triazacyclononane complexes as models for Binuclear Iron Centers in Biology - Properties of the Mixed-Valence Diiron(II,III) Species. *J. Am. Chem. Soc.* **1987**, *109*, 7387-7396.
108. Mashuta, M. S.; Webb, R. J.; Oberhausen, K. J.; Richardson, J. F.; Buchanan, R. M.; Hendrickson, D. N., Valence detrapping in iron(II)-iron(III) models of iron-oxo proteins. *J. Am. Chem. Soc.* **1989**, *111*, 2745-2746.
109. Payne, S. C.; Hagen, K. S., Steric control of reactivity of non-heme μ-hydroxo diiron(II) complexes with oxygen: Isolation of a strongly coupled μ-oxo Fe(II)Fe(III) dimer. *J. Am. Chem. Soc.* **2000**, *122*, 6399-6410.
110. Chuang, C.-H.; Liaw, W.-F.; Hung, C.-H., Conversion of Nitric Oxide into Nitrous Oxide as Triggered by the Polarization of Coordinated NO by Hydrogen Bonding. *Angew. Chem. Int. Ed.* **2016**, *55*, 5190-5194.

Table of Contents Figure.

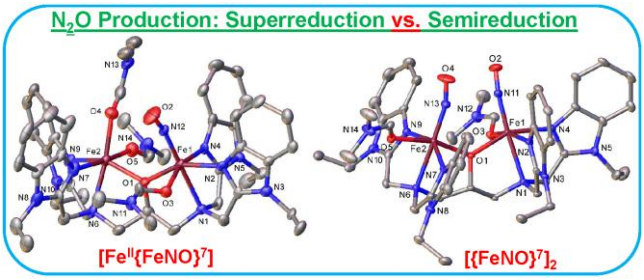

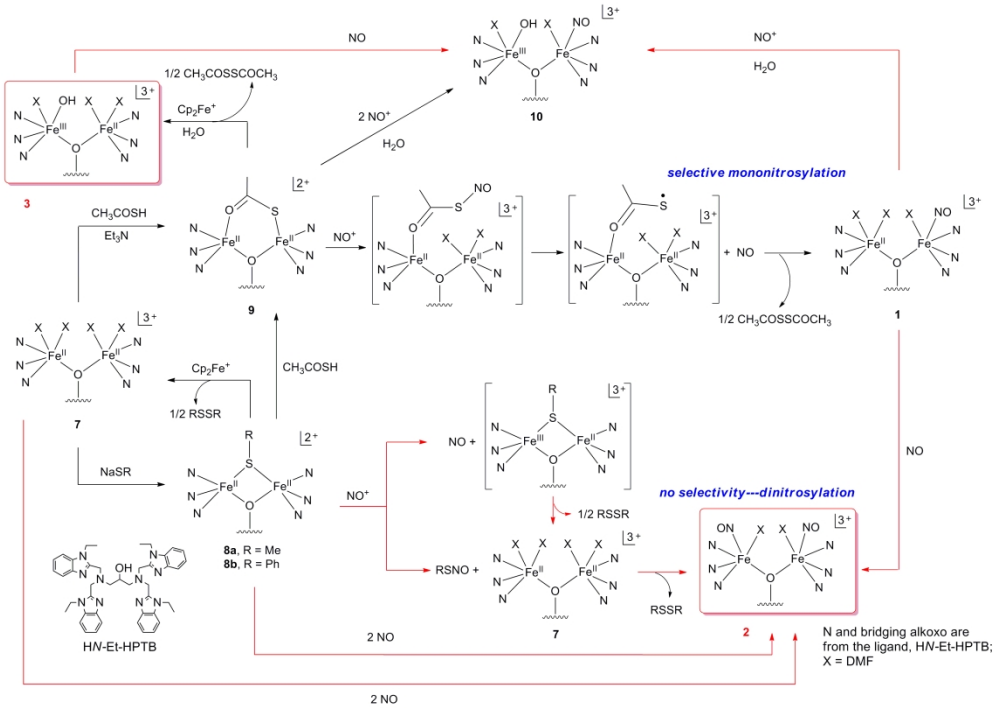

Scheme 1. Schematic presentation of the synthesis and reactivity of **1**–**3**. Ph_3CSNO and $(NO)(BF_4)$ were used as the sources of NO and NO^+, respectively. Possible reaction intermediates (not isolated) are shown in brackets. The new complexes, 2 and 3, and the new reactions are marked with red color. Complexes **1**; **9**;[55] **7**;[73] **8a**, **8b**;[74] and **10**[75] have been reported previously.

300x212mm (300 x 300 DPI)

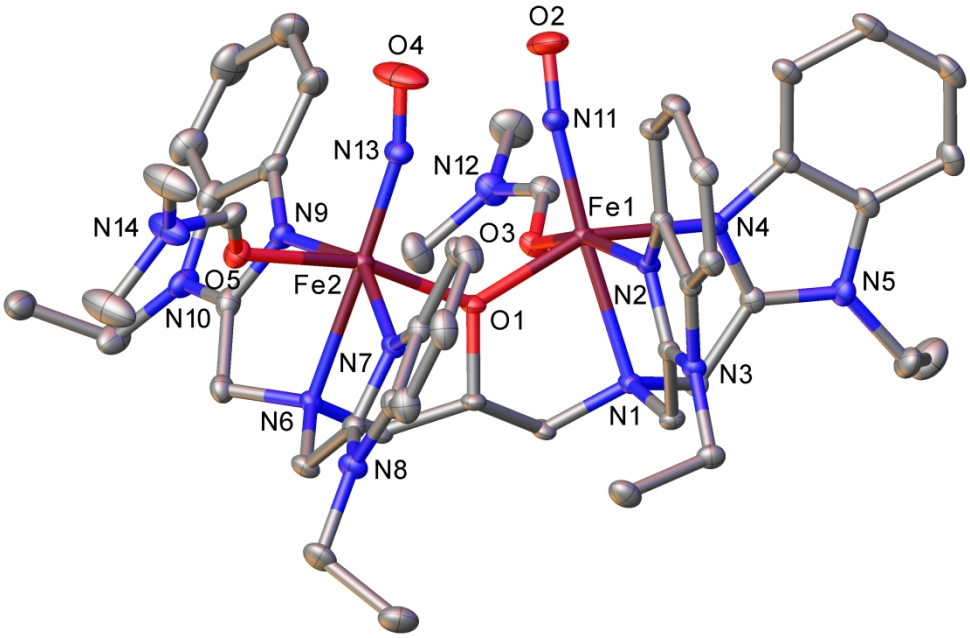

Figure 1. Molecular structure of **2** with 30% probability thermal ellipsoids and partial atom labeling scheme shown. Hydrogen atoms are omitted for clarity.

1128x749mm (72 x 72 DPI)

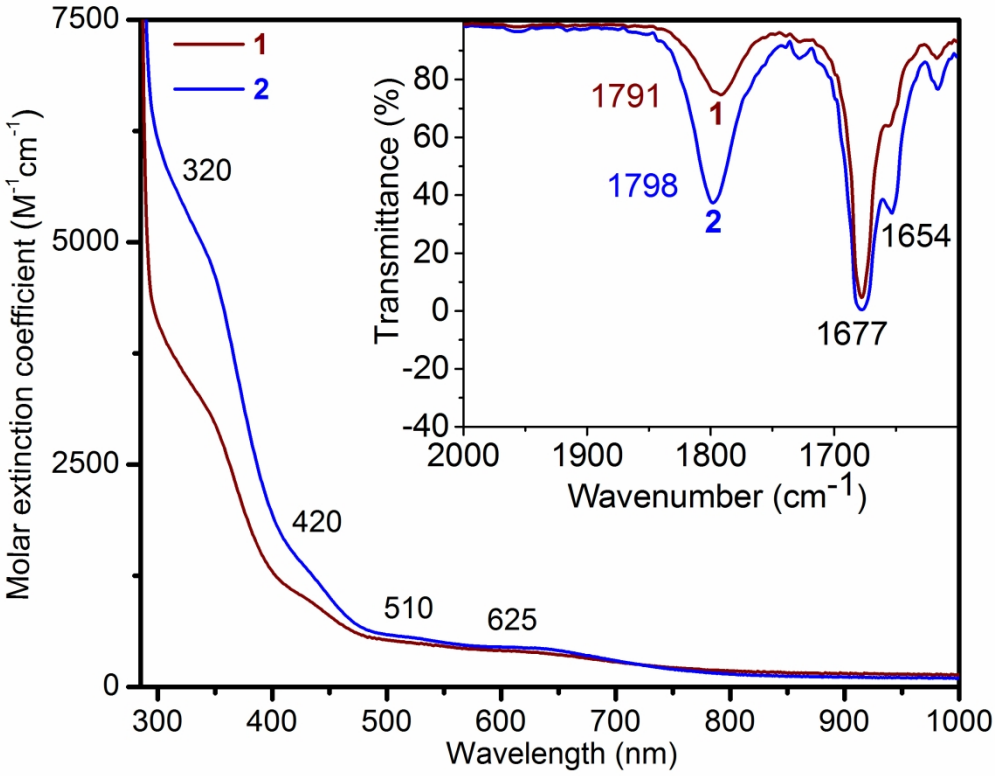

Figure 2. Electronic absorption and IR spectra of **1** and **2** in MeCN. [**1**] = [**2**] = 0.2 mM (UV-Vis) and 2 mM (IR).

232x180mm (300 x 300 DPI)

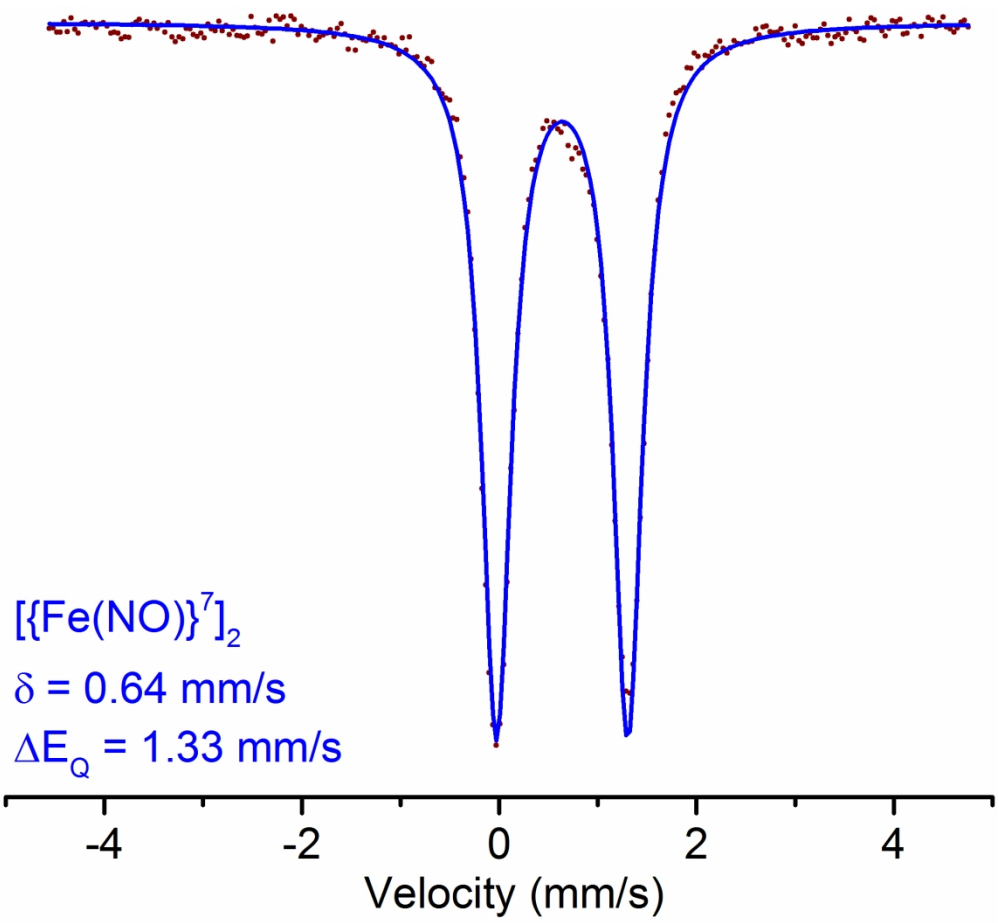

Figure 3. ^{57}Fe Mössbauer spectrum of a polycrystalline sample of **2** at 80K.

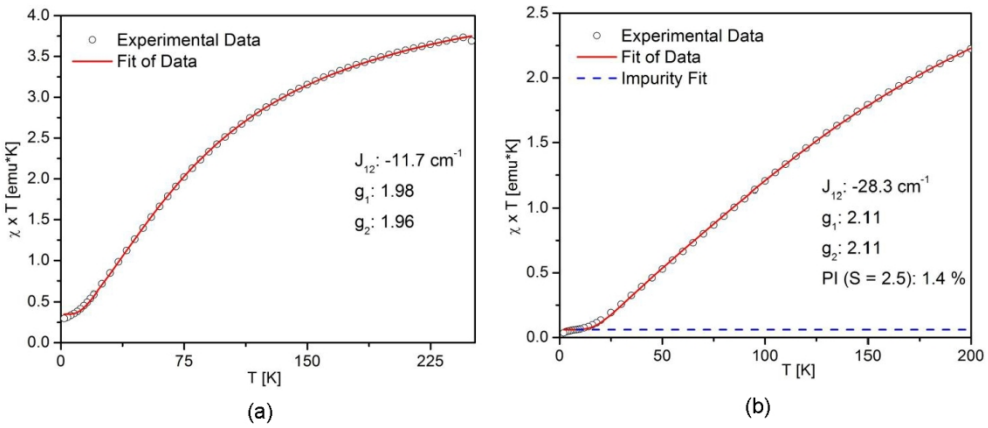

Figure 4. SQUID magnetometry measurements of **1** (a) and **2** (b). The solid red lines represent the best fits using S_1 = 3/2 and S_2 = 2 for **1** and S_1 = S_2 = 3/2 for **2** (see text).

192x84mm (200 x 200 DPI)

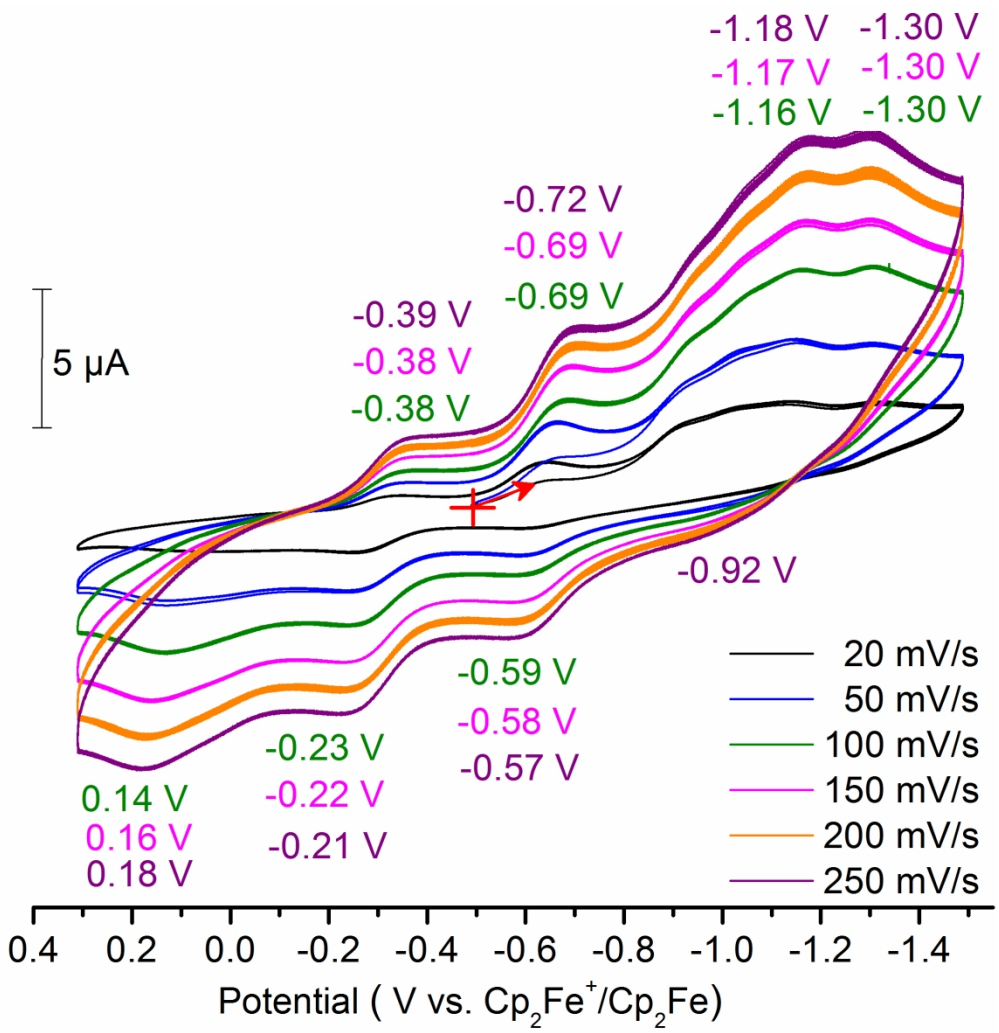

Figure 5. Cyclic voltammetry traces for **2** (multiple scans for each of the six different scan rates are shown) in DMF.

194x200mm (300 x 300 DPI)

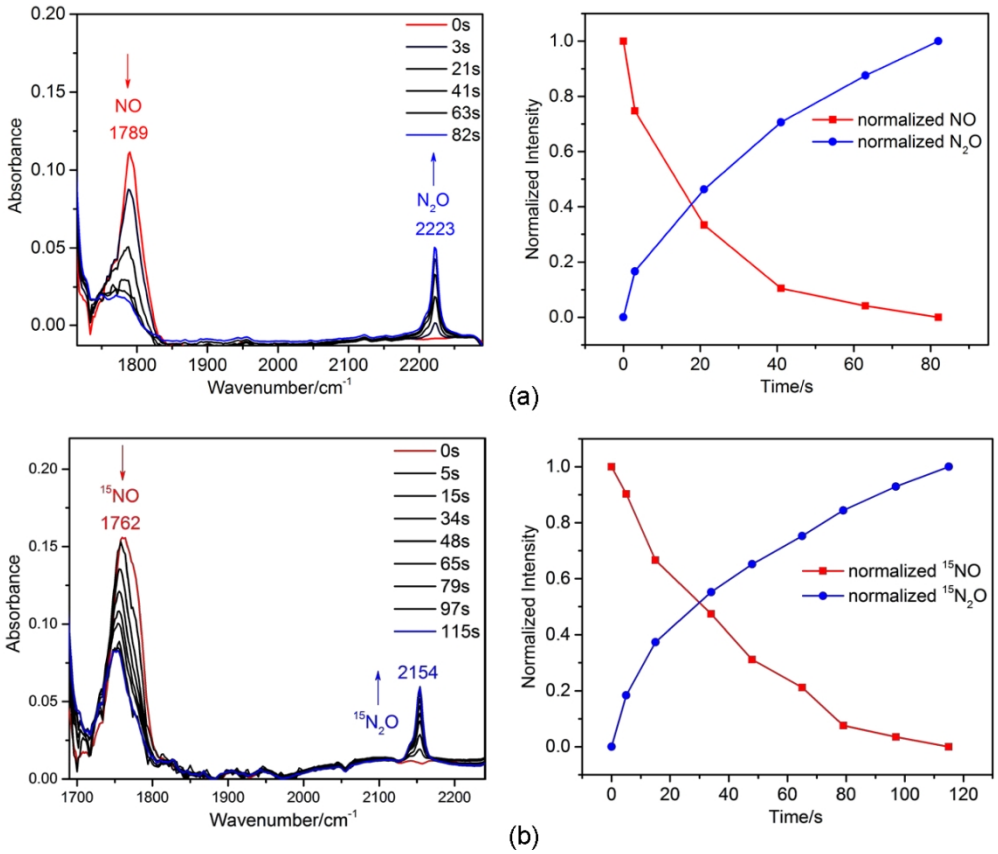

Figure 6. Generation of N_2O upon electrochemical reduction of **2** (a) and **2**(^{15}NO) (b).Conditions: [**2**] = 7.7 mM; [**2**(^{15}NO)] = 11.4 mM; hold potential at −1.6 V vs Ag wire; CH_2Cl_2, 0.1 M $(Et_4N)(BF_4)$.

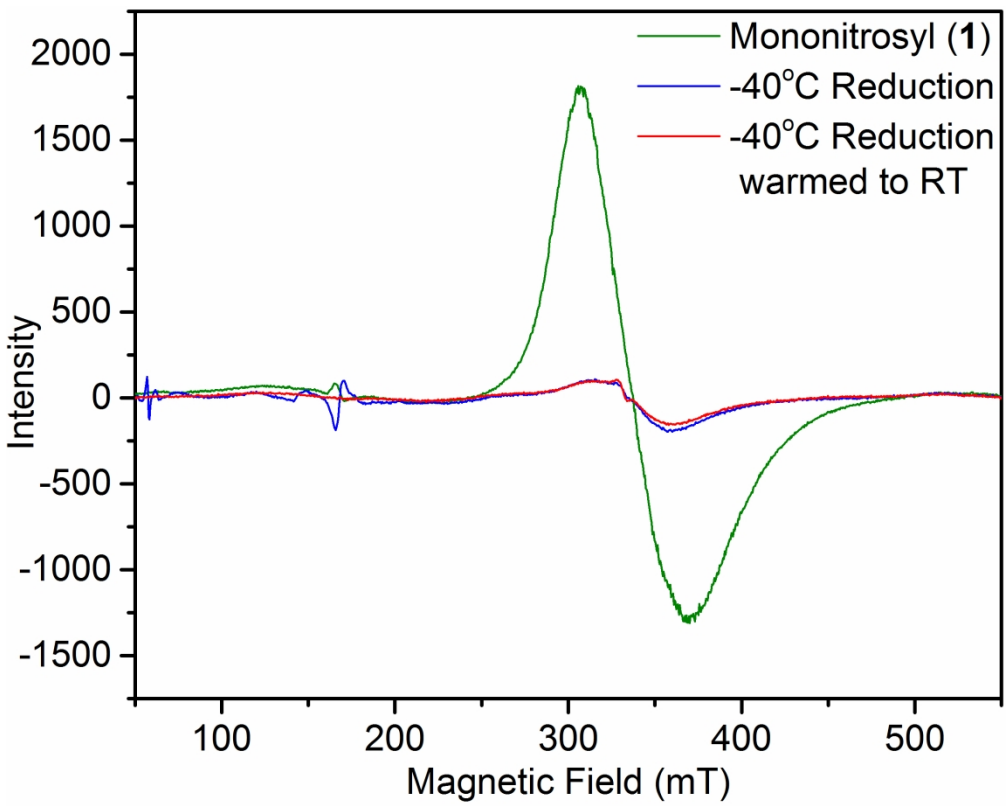

Figure 7. EPR study for the reaction of the mononitrosyldiiron(II) complex, **1** (<g> = 1.97), with excess Cp_2Co in MeCN. Conditions: [**1**] = ~2mM, [Cp_2Co] = ~4 mM, 9.355 GHz microwave frequency, 20.510 mW microwave power, 1 G modulation amplitude and 10.24 ms time constant.

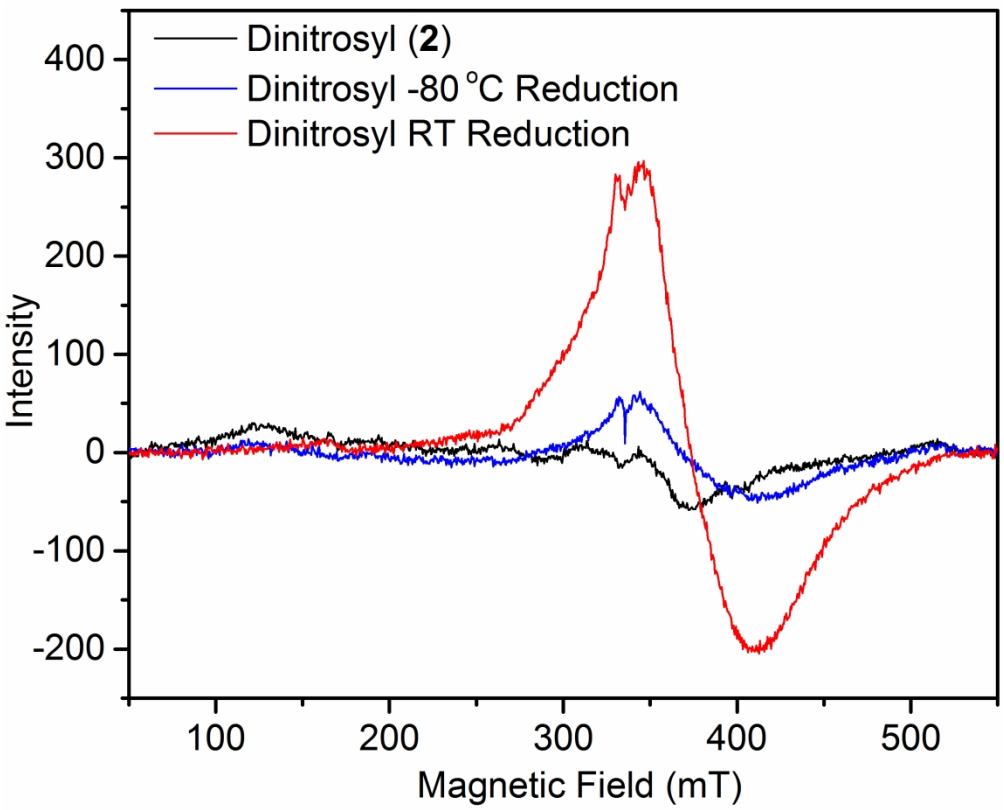

Figure 8. EPR study for the reaction of the dinitrosyl diiron(II) complex, **2** (black, 4.1 mM), with 1 eqv. Cp_2Co in CH_2Cl_2 at RT (red) and -80 oC (blue). Conditions for reduction at RT: [**2**] = 5.1 mM, [Cp_2Co] = 5.5 mM, 9.326 GHz microwave frequency, 20.460 mW microwave power, 1 G modulation amplitude and 10.24 ms time constant. Conditions for reduction at LT (−80 °C): [2] = 5.4 mM, [Cp2Co] = 5.5 mM, 9.336 GHz microwave frequency, 20.510 mW microwave power, 1 G modulation amplitude and 10.24 ms time constant.

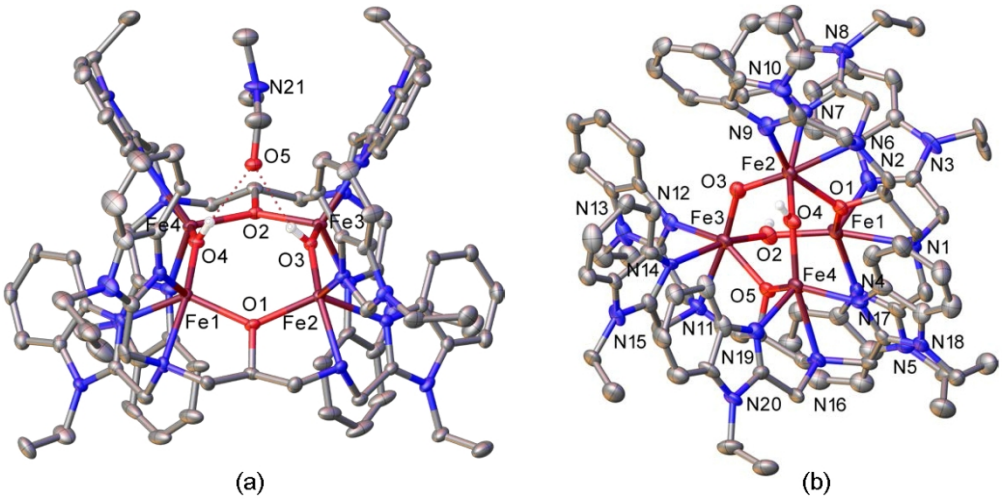

Figure 9. Molecular structures of (a) **11** and (b) **12** with 30% probability thermal ellipsoids and partial atom labeling scheme shown. Hydrogen atoms (except for the μ_2-OH groups) are omitted for clarity. Selected distances (Å): for **11**, Fe1-O2 = 2.018(9), Fe3-O2 = 1.980(8), Fe2-O4 = 1.999(9), Fe4-O4 = 1.985(8), Fe2-O3 = 1.814(8), Fe3-O3 = 1.816(8); for **12**, Fe1-O4 = 1.984(5), Fe4-O4 = 1.988(5), Fe3-O3 = 1.994(6), Fe2-O3 = 1.987(5). Selected angles (°): for **11**, <Fe1-O2-Fe3 = 120.9(4), <Fe2-O4-Fe4 = 120.6(4), <Fe2-O3-Fe3 = 130.2(5); for **12**, <Fe1-O4-Fe4 = 142.5(3), <Fe2-O3-Fe3 = 146.2(3).

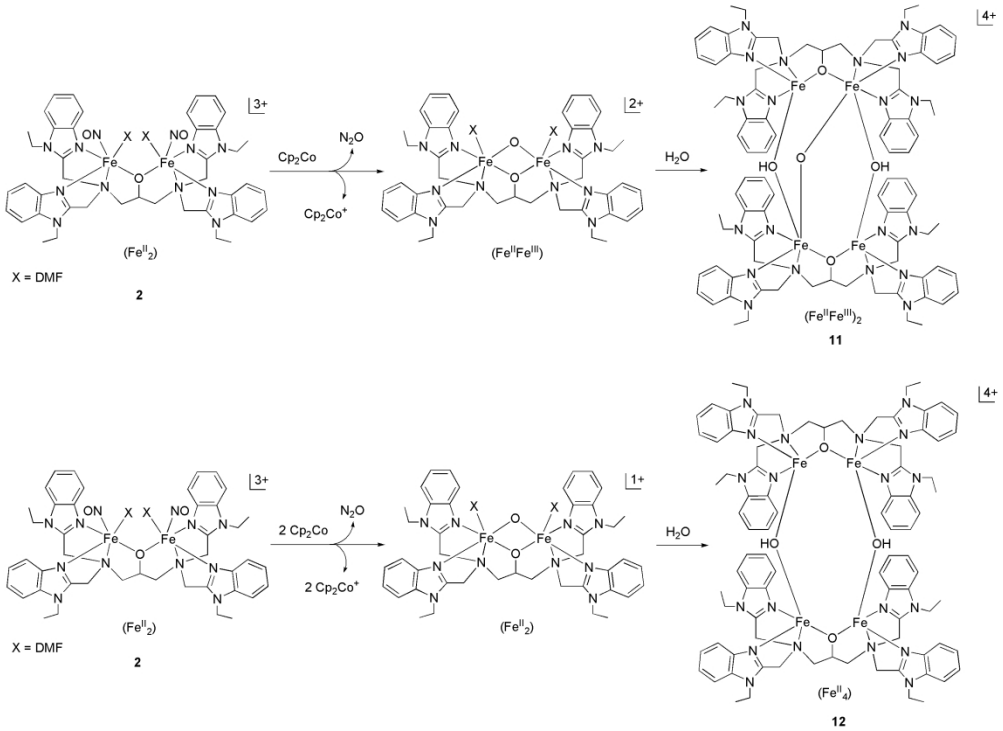

Scheme 2. Schematic presentation of the mechanism for the generation of N_2O upon reduction of **2** by 1 and 2 equivalents of cobaltocene. Complexes **2**, **11** and **12** have been characterized by single crystal x-ray structure determinations.

273x198mm (300 x 300 DPI)

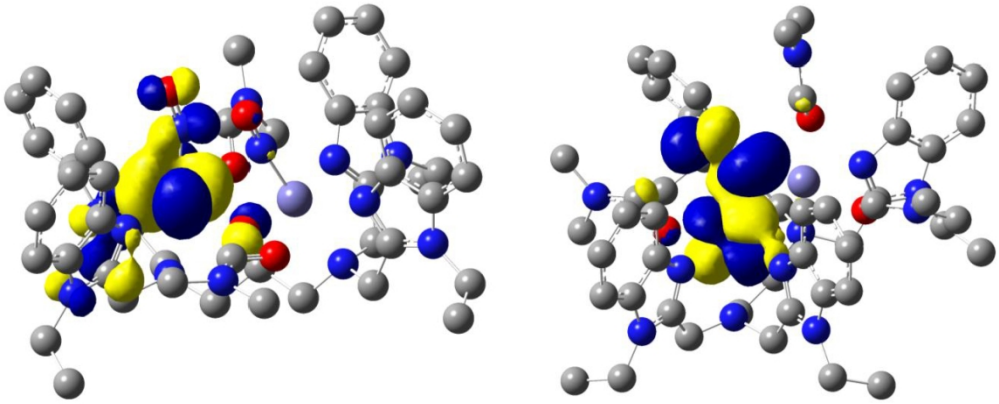

Figure 10. (Left) Contour plot of the non-bonding dxy orbital (with respect to NO) that is occupied upon one-electron reduction of 2^{3+} to 2^{2+}. Note that since the coordination environment of the two $\{FeNO\}^7$ units in 2^{3+} is identical, with the amine groups trans to NO in both cases, reduction of the other iron center gives the same result. (Right) Contour plot of the antibonding dxz orbital (with respect to NO) that is occupied upon reduction of 1^{3+} to 1^{2+}.

168x70mm (200 x 200 DPI)

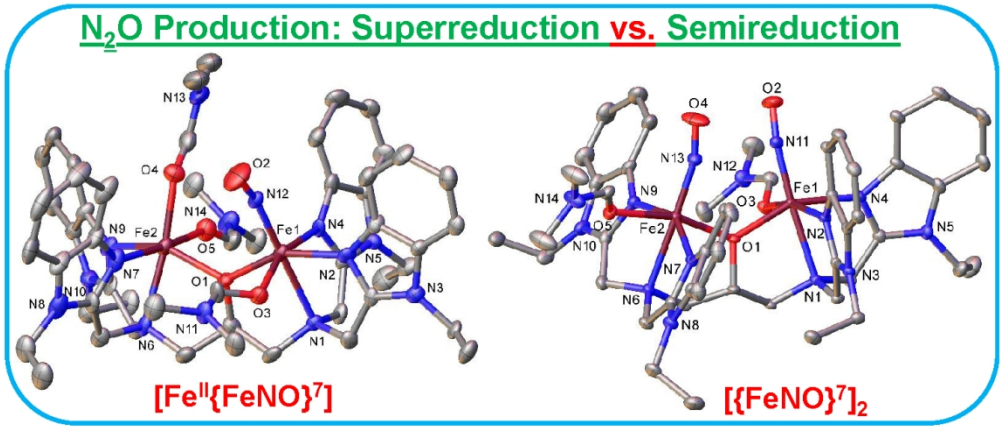

188x80mm (200 x 200 DPI)